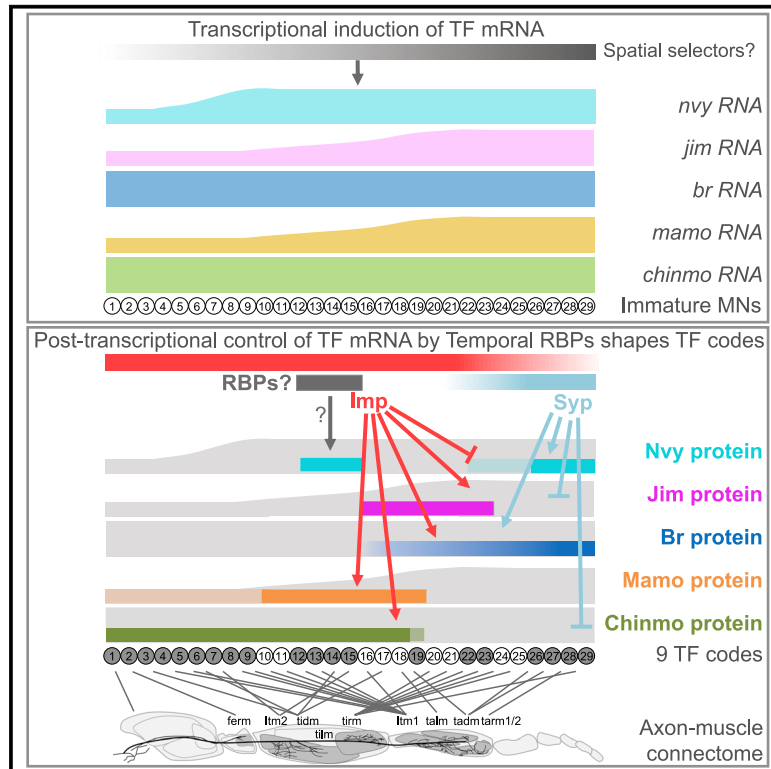


Post-transcriptional regulation of transcription factor codes in immature neurons drives neuronal diversity

Graphical abstract



Authors

Wenyue Guan, Stéphanie Bellemin, Mathilde Bouchet, ..., Séverine Urdy, Richard S. Mann, Jonathan Enriquez

Correspondence

jonathan.enriquez@ens-lyon.fr

In brief

Guan et al. discovered that the individual morphological fates of motoneurons are determined by the transcription factor mRNAs they express together with gradients of RNA-binding proteins that determine which TF mRNAs are translated, ultimately producing a set of TF codes that are unique for each neuron.

Highlights

- 29 leg MNs from the same neuroblast express 19 combinations of TFs (TF codes)
- The TF codes are expressed as a function of MN birth order
- Imp and Syp post-transcriptionally regulate at least five TFs
- Changing Imp and Syp level modifies nine TF codes and the axonal targeting accordingly



Article

Post-transcriptional regulation of transcription factor codes in immature neurons drives neuronal diversity

Wenyue Guan,¹ Stéphanie Bellemin,^{1,4} Mathilde Bouchet,^{1,4} Lalanti Venkatasubramanian,^{2,4} Camille Guillermin,¹ Anne Laurençon,¹ Chérif Kabir,¹ Aurélien Darnas,¹ Christophe Godin,³ Séverine Urdy,¹ Richard S. Mann,² and Jonathan Enriquez^{1,5,*}

¹Institut de Génomique Fonctionnelle de Lyon, UMR5242, Ecole Normale Supérieure de Lyon, Centre National de la Recherche Scientifique, Université Claude Bernard-Lyon 1, 46 Allée d'Italie, 69364 Lyon Cedex 07, France

²Departments of Biochemistry and Molecular Biophysics, and Neuroscience, Mortimer B. Zuckerman Mind Brain Behavior Institute, Columbia University, New York, NY 10027, USA

³Laboratoire Reproduction et Développement des Plantes, Univ Lyon, ENS de Lyon, UCB Lyon 1, CNRS, INRA, Lyon, France

⁴These authors contributed equally

⁵Lead contact

*Correspondence: jonathan.enriquez@ens-lyon.fr
<https://doi.org/10.1016/j.celrep.2022.110992>

SUMMARY

How the vast array of neuronal diversity is generated remains an unsolved problem. Here, we investigate how 29 morphologically distinct leg motoneurons are generated from a single stem cell in *Drosophila*. We identify 19 transcription factor (TF) codes expressed in immature motoneurons just before their morphological differentiation. Using genetic manipulations and a computational tool, we demonstrate that the TF codes are progressively established in immature motoneurons according to their birth order. Comparing RNA and protein expression patterns of multiple TFs reveals that post-transcriptional regulation plays an essential role in shaping these TF codes. Two RNA-binding proteins, Imp and Syp, expressed in opposing gradients in immature motoneurons, control the translation of multiple TFs. The varying sensitivity of TF mRNAs to the opposing gradients of Imp and Syp in immature motoneurons decrypts these gradients into distinct TF codes, establishing the connectome between motoneuron axons and their target muscles.

INTRODUCTION

Locomotion is a stereotyped behavior used by animals to find food, mates, or escape from predators. The rhythmic and precise pattern of locomotion is linked to the coordinated contraction of muscles that are innervated by a complex wiring of motoneuron (MN) axons controlling the timing and the intensity of muscle activity. One central challenge is to decipher how stem cells generate a huge diversity of MN morphologies. Here, we used a combination of genetic and computational approaches to understand how, in *Drosophila*, a single stem cell gives rise to 29 morphologically unique MNs.

Transcription factors (TFs) are central regulators of the morphological specification of neurons, including MNs. In vertebrates, during development, Hox6 and Hox10 paralogs at the brachial and lumbar levels of the spinal cord distinguish MNs that target leg muscles from those that target body wall muscles. Subsequently, limb-targeting MNs are further refined into pools, where all MNs in a single pool target the same muscle. Each pool is molecularly defined by the expression of pool-specific TFs (Dasen and Jessell, 2009; Philippidou and Dasen, 2013). In *Drosophila* embryos, subclasses of MNs innervating the larva

body-wall muscles are also morphologically specified by unique combinations of TFs controlling ventral versus dorsal targeting (Fujioka et al., 2003; Garces and Thor, 2006; Landgraf et al., 1999; Broihier and Skeath, 2002; Broihier et al., 2004; Certel and Thor, 2004; Oyallon et al., 2012; Thor and Thomas, 1997; Thor et al., 1999). The morphological specification of *Drosophila* leg MNs seems to be controlled at the single-cell level by a combination of morphology-specifying TFs (mTFs). Seven MNs innervating limb appendages differentially express unique combinatorial codes of five mTFs that determine most of their morphological fates (Enriquez et al., 2015).

Immature neurons expressing the TF codes are generated by dedicated stem cells. These stem cells are regulated in space and time to generate an enormous amount of morphological diversity at the right time and in the right place (Kohwi and Doe, 2013; Sagner and Briscoe, 2019). *Drosophila* neurons are generated by neuroblasts (NBs), specialized stem cells dedicated to the generation of neurons and glia (Doe and Skeath, 1996; Prokop and Technau, 1991; Truman and Bate, 1988). As they divide, NBs express a temporal sequence of TFs (tTFs) that contribute to the generation of neuronal diversity. In the embryonic ventral nerve cord (VNC) (analogue of the human spinal cord), most



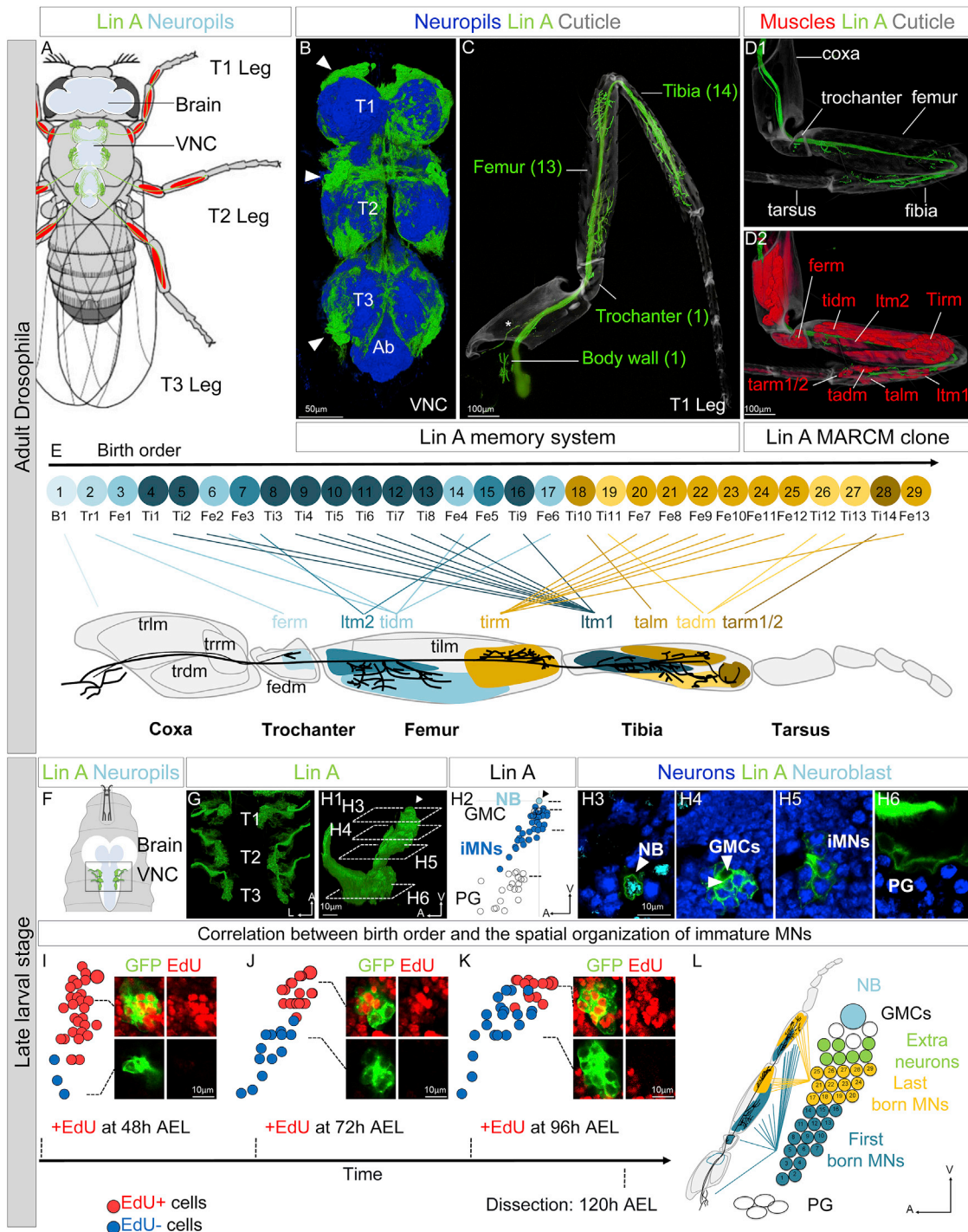


Figure 1. Lin A, a model to study how the MN-muscle connectome is built

(A) Drawing of a fly showing the CNS and Lin A/15 MNs.

(B) VNC with six Lin A/15 labeled with myr::GFP (green) and immunostained with anti-BRP (blue). Arrowheads indicate MN cell bodies.

(C) T1 leg with Lin A/15 axons labeled with myr::GFP (green).

(D) T1 leg with a Lin A/15 MARCM clone expressing mCD8::GFP (green) and all muscles were labeled with *Mhc-RFP* (red). The number of MNs innervating the corresponding leg segment are indicated in (C). Leg muscles innervated by Lin A/15 are indicated in (D2).

(E) Schematic showing the link between birth order and muscle targeting, modified from Baek and Mann (2009) (see link between birth order and muscle targets in STAR Methods). Top: schematic of the cell body of Lin A/15 iMNs is shown. The numbers inside indicate their birth order, and the abbreviations below indicate the name of the MNs based on the nomenclature from Baek and Mann (2009). Bottom: schematic of a T1 leg innervated by Lin A/15 is shown; the muscles innervated

(legend continued on next page)

NBs express a sequence of five tTFs (Isshiki et al., 2001; Li et al., 2013a), whereas in medulla NBs of the visual system and intermediate neural progenitors of the *Drosophila* larval brain, a different series of tTFs have been described (Bayraktar and Doe, 2013; Konstantinides et al., 2022; Li et al., 2013b). In vertebrates, neural stem cells, e.g., in the cerebral cortex, retina, and spinal cord, use analogous strategies, suggesting that the regulatory logic of tTFs is evolutionarily conserved (Alsiö et al., 2013; Delile et al., 2019; Elliott et al., 2008; Jacob et al., 2008; Mattar et al., 2015; Okano and Temple, 2009).

In *Drosophila*, neuronal diversity can be generated by NBs as they age via a second mechanism involving two RNA-binding proteins (RBPs), insulin growth factor (IGF)-II mRNA-binding protein (Imp) and Syncrip (Syp). These RBPs are expressed in opposing temporal gradients in brain NBs from high to low and low to high, respectively (Liu et al., 2015; Ren et al., 2017; Syed et al., 2017). In the NBs of the mushroom body, a structure in the brain processing olfactory inputs, these two RBPs regulate the translation of the TF Chinmo, which in turn controls the temporal identity of the mushroom-body NB progeny in a concentration-dependent manner. This gradient strategy allows the generation of many neurons of the same type, within a particular time window, as observed in mammalian progenitors.

Here, we used a lineage called Lin A/15 that produces 29 of the ~50 MNs with unique morphologies (Baek and Mann, 2009; Enriquez et al., 2018) as a model and discovered a mechanism controlling the generation of a large amount of neuronal diversity in a short time window by a single stem cell. We report the discovery of 16 TFs expressed in combination and determining 19 different TF codes in immature MNs (iMNs) just before their morphological differentiation. These TF codes are not established at the birth of the iMNs but are gradually shaped during development. By comparing the expression profile of six mRNAs with their corresponding proteins, we revealed that post-transcriptional regulation of TFs plays a key role in shaping the TF codes. We then examined the function of two known RBPs, Imp and Syp, in shaping the TF code in iMNs. We first demonstrated that, in earlier born iMNs, Syp protein was undetectable and the level of Imp was high, whereas in the later born iMNs, the level of Syp protein was high and Imp was low. We discovered that this opposite expression pattern in iMNs of both RBPs is essential to shape the axon-muscle connectome by regulating the translation of at least five TFs examined. Finally, we revealed that Imp controls the fate of the Lin A/15 progenies directly in iMNs. With these results, we propose a model where RBPs act as temporal factors

to specify the fate of iMNs by post-transcriptionally sculpting a complex set of TF codes.

RESULTS

Lin A/15, a model to study how the MN-muscle connectome is built during development

Previous studies have characterized the morphologies of individual Lin A/15 MNs by MN-driven GFP labeling, whereby the presumptive muscle target is identified through the localization of the terminal branches in the leg (Baek and Mann, 2009; Brierley et al., 2009, 2012).

Here, we extend these earlier studies by driving the expression of RFP in all leg muscles (*Mhc-RFP*), in addition to driving the expression of GFP in 28 Lin A/15 MNs with the MARCM technique (Lee and Luo, 1999; Figure 1D). Lin A/15 MNs innervate 9 out of the 14 leg muscles: all five muscles in the tibia, three muscles in the femur, and one muscle in the trochanter. The first-born MN from Lin A/15, which cannot be visualized with the “one-spot” MARCM technique (see STAR Methods), innervates a body-wall muscle and can be genetically labeled with GFP by using a Lin A/15 tracing system (Figures 1A–1C; see STAR Methods). Based on this and previous studies, the tight correlation between the birth order of Lin A/15 MNs and their muscle targets can be schematically summarized (Figure 1E; see STAR Methods).

Correlation between birth order and the spatial organization of iMNs

The late third instar (L3) is a key developmental stage between the end of MN production and the establishment of axon-muscle connections (Baek et al., 2013; Venkatasubramanian et al., 2019). We thus chose this stage as an entry point to understand how MN diversity is generated.

We first determined how the spatial organization of iMNs is related to birth order (Figures 1F–1K). In late L3, the NB has a ventral location, whereas iMNs are located more dorsally and anteriorly (Figures 1G and 1H). When larvae are fed with the DNA-label EdU at early time points, the last-born MNs (EdU⁺) are located ventrally and posteriorly near to the NB, whereas older MNs (EdU[−]) are located dorsally and anteriorly distant from the NB. Moreover, EdU⁺ iMNs and EdU[−] iMNs are barely intermingled (Figures 1I–1K). This demonstrates that, up to the end of L3, iMNs maintain distinct spatial positions that are dictated by their birth dates. Importantly for our study, the most ventral iMNs, which are the last-born iMNs, undergo

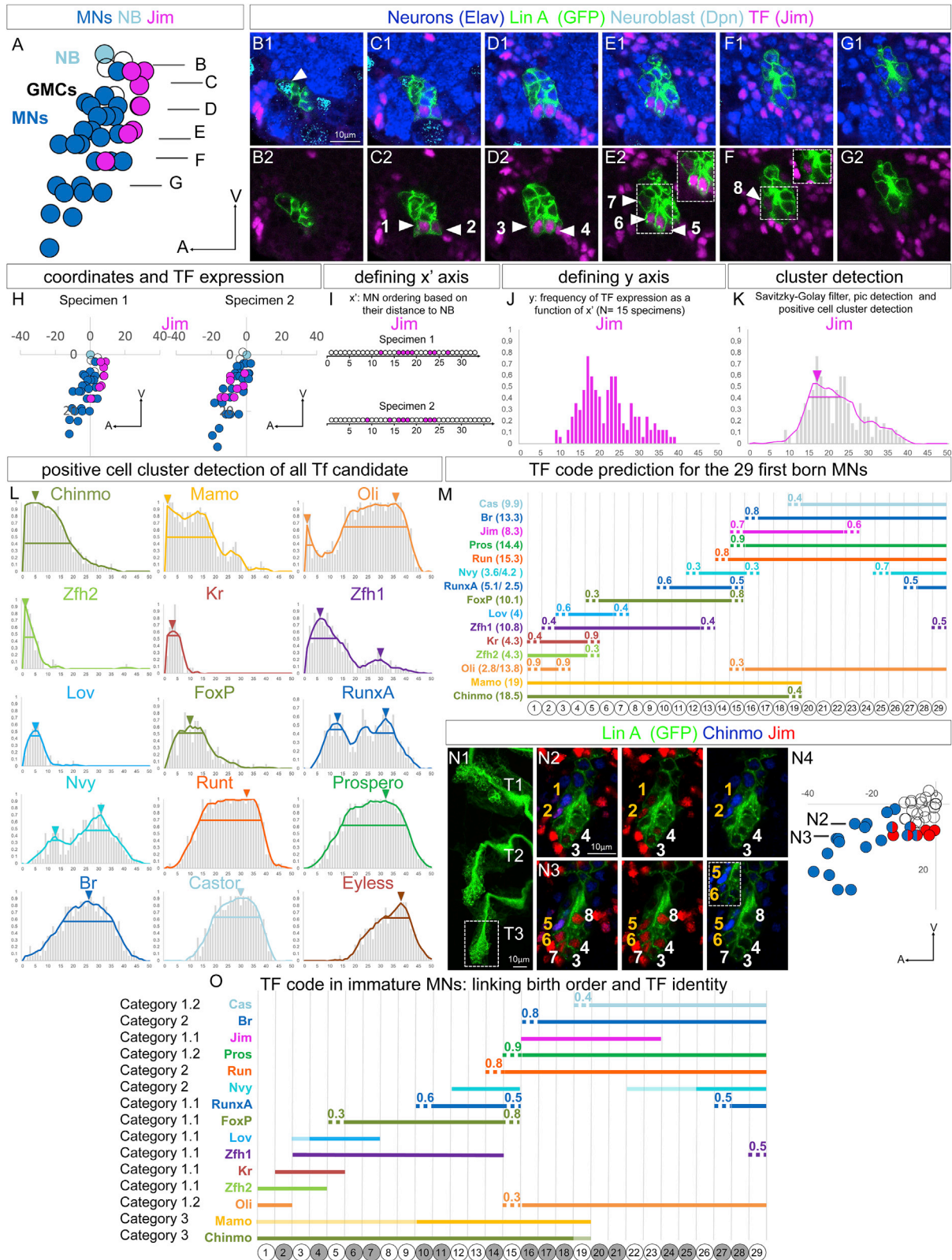
by Lin A/15 are color coded based on their innervation. The line between the cell body and leg muscles indicates the relationships between MN birth order and muscle innervation. Muscle nomenclature is based on Soler et al. (2004): d, depressor; fe, femur; l, levator; m, muscle; r, reductor; t, tendon; ta, tarsus; ti, tibia; tr, trochanter.

(F) Drawing of the anterior region of an L3 larva showing the CNS and Lin A/15 iMNs.

(G and H) 3D reconstruction of six (G) and one (H1) right thoracic hemisegment 2 (T2R) Lin A/15 in an L3 larva labeled with myr:GFP (green). Ventral (G) and lateral (H1) views are shown; axes: A, anterior; L, lateral; V, ventral. (H2) Plot of the relative position of each Lin A/15 cell in (H1) from a lateral perspective is shown. Lin A/15 proliferative glia (PG) are in white, iMNs are in blue, GMCs are in white, and the NB is in cyan. (H3–H6) Confocal sections of the Lin A/15 in (H1) and (H2) immunostained with anti-Elav (blue) and Dpn (cyan).

(I–K) Plots of the relative position of each Lin A/15 cell from a lateral perspective in L3 larvae fed with EdU at indicated time points: EdU⁺ cells (red) and EdU[−] cells (blue). The horizontal axis indicates the time point of EdU feeding. On the right of each graph, confocal sections of Lin A/15 are shown.

(L) Schematic of Lin A/15 cell bodies in an L3 larva and of an adult leg that shows the correlation between the position of the iMNs and the muscle targeting of adult MNs.



(legend on next page)

apoptosis during the pupal stages (Guan et al., 2021), whereas the first-born 29 iMNs morphologically differentiate during metamorphosis (Figure 1L). This clear relationship between birth order and the spatial organization of iMNs was then used to understand how iMNs are morphologically specified by TFs.

A complex combination of TFs in iMNs prefigures morphological diversity of Lin A/15 MNs

To identify the TFs expressed in Lin A/15 iMNs at late L3 that could control the stereotypic wiring of muscle innervation, we performed an immunostaining screen of GFP-expressing iMNs with a collection of around 220 antibodies directed against different TFs, covering ~35% of all TFs coded by the *Drosophila* genome. In total, 45 TFs were identified in Lin A/15, with 16 TFs expressed in different subpopulation of iMNs (Figures 2A–2G illustrates the example of Jim and Figure S1 other TFs). We then focused our study on these 16 TFs, since their differential expressions could be at the origin of the large diversity of MN morphologies generated by Lin A/15 NB.

We therefore developed a method based on the correlation between the relative position of iMNs from Lin A/15 NB and their birth order to assign the correct combination of TFs to each iMN (see STAR Methods). We named this method the positive cell cluster detection (PCCD) method. In this method, x, y, and z coordinates and on and off expression of a given TF were assigned to each Lin A/15 iMN for at least 15 Lin A/15 samples per immunostaining (Figure 2H illustrates two Lin A/15 samples with anti-Jim immunostaining). With these coordinates, each Lin A/15 iMN is ranked along an x' axis according to its relative distance from the NB, such that the lowest rank (1) corresponds to the greatest distance from the NB (Figure 2I illustrates the iMN ranking of two samples of anti-Jim immunostaining). Then, the frequency of TF expression is calculated as a function of x' (Figure 2J illustrated frequency of Jim expression in 15 samples analyzed). The distributions of frequencies are smoothed by application of a Savitzky-Golay filter. The peak of each distribution is identified, and the positive cell cluster of iMNs associated with each peak

is assigned (Figure 2K illustrates the identification of iMN cluster expressing Jim; Figure 2L shows similar cluster predictions for all other TFs). We schematized our results for the 29 first-born iMNs on a birth-order axis in order to predict the combination of TFs expressed in each iMN, since there is a correlation between MN birth order and their relative distance to the NB (x' axis). PCCD reveals that 15 out of the 16 differentially expressed TFs are expressed in combinations in the 29 first-born Lin A/15 iMNs (Figure 2M). One TF (Eyeless) was only expressed in the supernumerary iMNs eliminated by apoptosis during pupal stages (Guan et al., 2021). To validate and refine this analysis, 12 co-immunostainings for different TFs were performed (Figure 2N illustrates Chinmo and Jim co-staining; Figure S2 shows all co-stainings). The result of the co-stainings reveals that PCCD is very accurate, because in most cases, none or only one cell correction was required (STAR Methods; compare Figure 2M versus Figure 2O). In summary, we could assign 19 different TF codes for 29 iMNs: 10 iMNs shared unique TF codes, 16 iMNs share a code with other iMNs born sequentially, and 3 iMNs born in the same time window have similar codes (Figure 2O).

TF-code diversity is progressively established in iMNs

We then determined how the expression pattern of the 15 differentially expressed TFs is established by analyzing their expression from the end of L2, when the NB begins to proliferate, until late L3.

We classified Lin A/15 TFs into three categories based on their spatial and temporal expression dynamics. The first category encompasses 10 TFs whose expression starts in the ganglion mother cell (GMC) or postmitotic neurons (Figures 3A–3H and S3; note that Pros and FoxP were placed in this category, even though they were also detected in the NB cytoplasm). The expression dynamics of the TFs in this category were further subdivided into two sub-categories based on their temporal expression dynamics. Category 1.1 is composed of seven TFs expressed and maintained by subpopulations of iMNs since their birth (Lov, RunxA, Zfh2, Kr, and Zfh1) or whose expression turns

Figure 2. Correlation between birth order and TF codes

(A–G) Plot (A) of the relative position of each Lin A/15 cell from a lateral perspective and confocal sections (B1–G2) in an L3 larva immunostained with anti-Jim (purple), anti-Elav (blue), and anti-Dpn (cyan) and where Lin A/15 is labeled with myr:GFP (green). Black lines in (A) indicate the positions of the confocal section in (B1)–(G2) (see Figure S1 for the expression pattern of all TFs).

(H) On the left (specimen 1), same graph as in (A) but where the spatial axis is represented (units are in micrometer). On the right, graph from another specimen (specimen 2) is shown.

(I) MN ordering on an x' axis according to their relative distance from the NB; Jim⁺ iMNs are in purple.

(J and K) Frequency of Jim expression as a function of x' among 15 specimens before (J) and after (K) applying a Savitzky-Golay filter. (K) The arrow indicates the peak of the Jim⁺ cell cluster. The horizontal bar indicates the Jim⁺ cell cluster detected with the PCCD method (see STAR Methods).

(L) Same plot as in (K) for 15 TFs.

(M) Schematic of the TF codes expressed in each iMN predicted by the PCCD method in an L3 larva. Bottom: schematic of the cell body of Lin A/15 iMNs is shown. The numbers inside indicate their relative distances from NB. Top: the horizontal bars indicate the TF⁺ cell clusters detected with the PCCD method. The dotted lines indicate the coverage index at the border. The numbers in parentheses indicate the length of the TF-positive cell clusters (see STAR Methods).

(N) Three thoracic hemisegments (T1–T3) (N1) and two confocal (N2 and N3) sections of the dotted box in (N1) in an L3 CNS with a myr:GFP⁺ Lin A/15 (green) immunostained with anti-Jim (red) and anti-Chinmo (blue). The numbers in white and orange indicate the Jim⁺ iMNs and the Jim⁺ and Chinmo⁺ iMNs, respectively. The position of the confocal sections is indicated in (N4). (N4) Plots of the relative position of the Lin A/15 corresponding to the Lin A/15 boxed in (N1) are shown. One out of the four Jim⁺ Chinmo⁺ cells expressed a very low level of Chinmo (number 6 in N3) (see Figure S2 for all co-stainings). For each co-staining, a minimum of 10 Lin A/15 samples are analyzed.

(O) Same schematic as in (M) after validation and small corrections of the PCCD method by performing co-staining (see STAR Methods). TF gradient expressions of Castor, Br, Runt, Pros, and Oli were not taken into consideration when assigning the codes. The weak expression of Chinmo, Nvy, and Mamo is indicated in lighter colors. The color of the Lin A/15 iMN cell bodies change from white to gray at each switch to a new TF code. The name of the categories to which a TF belongs is indicated on left (see Figure 3).

on after a delay (Jim and FoxP) (Figures 3A–3D and S3). Three TFs from the other sub-category (category 1.2) are expressed in all new-born iMNs (Oli, Cas, and Pros). However, their expression is only maintained in a subpopulation of iMNs (Figures 3E–3H and S3). The second category (category 2) is composed of Br, Run, and Nvy, which are TFs expressed continuously in the Lin A/15 NB from late L2 until late L3. All new-born iMNs expressed these TFs, but their expression is maintained in different groups of iMNs (Figures 3I–3L and S3). Last, the third category (category 3) is composed by Chinmo and Mamo, which are the only TFs having a temporal expression in the NB (Figures 3M, 3P, and S3). As described for other lineages (Dillard et al., 2018; Maurange et al., 2008; Syed et al., 2017), Chinmo is expressed in the NB in early stages and only maintained in the first-born MNs. However, the expression of Mamo in the NB is completely uncoupled from its expression in iMNs, suggesting that Mamo function in NB versus MNs might not be linked (Figure S3).

These results showed that the TF codes are gradually established in iMNs by a *de novo* expression of TFs in GMCs and iMNs (category 1) and by the selective maintenance and/or repression of TFs in iMNs (categories 1, 2, and 3). These expression dynamics suggest the existence of upstream regulators shaping the TF codes by induction and maintenance and/or repressive mechanisms.

Post-transcriptional regulation governs the establishment of TF codes

In view of the complex dynamics of TF protein expression, we wondered to which extent it could be shaped by post-transcriptional regulation. To address this question, we analyzed the RNA expression pattern of six TFs selected as representatives of the protein-expression profiles categorized above: *jim* and *Oli* (category 1), *br* and *nvy* (category 2), and *mamo* and *chinmo* (category 3).

We performed single-molecule fluorescence *in situ* hybridization (smFISH) and developed a pipeline to quantify the number of RNA spots per Lin A/15 iMN in L3 VNC (Figures 4A–4I and S4). This pipeline combined 3D segmentation of Lin A/15 cells (Machado et al., 2019) and a computational quantification of the number of RNA spots in each Lin A/15 cell (Raj et al., 2008; see STAR Methods). The number (N) of RNA dots detected in each iMN as a function of the iMN's relative distance to the NB was calculated (Figures 4E–4I and S4). The number of RNA were also calculated for clusters of contiguous iMNs ($N^{x'-x''}$), where x' and x'' are the iMN furthest and closest to the NB in a selected cluster. For example, *jim* RNA was expressed at higher

levels in ventral (young) iMNs proximal to the NB ($N^{21-29} = 52$ and $N^{11-20} = 54$) than the dorsal (old) iMNs ($N^{1-10} = 27$) and was barely detectable in the NB ($N^{NB} = 9$). This ubiquitous expression of *jim* RNA from high to low in young and old iMNs, respectively, contrasts with the expression of the Jim protein detected in only eight iMNs (Figure 2) and not detected at all in young iMNs, including in the supernumerary MNs removed during pupal stages, where *jim* RNA is the most expressed (Figure 2 versus Figure 4). The RNA of *chinmo*, *mamo*, *br*, *nvy*, and *oli* were also present ubiquitously in iMNs, while the proteins were detected in subpopulation of iMNs (Figure 2 versus Figures 4F–4I and S4 and Table S1).

The comparison of the RNA expression pattern of six TFs with their respective proteins suggest that post-transcriptional regulation plays a key role in shaping TF codes in iMNs.

Opposite spatial gradients of Imp and Syp control the specificity of axonal targeting

To investigate further post-transcriptional regulation, we investigated the expression dynamics and function on muscle innervation of two known RBPs, Imp and Syp, that are major players in the temporal specification of VNC and central brain lineages in *Drosophila* (Liu et al., 2015; Ren et al., 2017; Syed et al., 2017). In Lin A/15 NB, both Imp and Syp proteins follow opposing temporal expression gradients in accordance with previously described studies of other NBs in the CNS (Guan et al., 2021).

In iMNs, Imp and Syp proteins have opposing gradients according to their birth date (Figure 4K). By analyzing the co-expression of Imp and Syp in iMNs with Jim (expressed in iMNs 16–23; Figures 2O and 4J), we concluded that Imp is highly expressed in iMNs 1–23 and weakly expressed in iMNs 24–29, whereas Syp is highly expressed in iMNs 24–29 in gradient manner and not detected in older iMNs (Figure 4L). Moreover, the detection of primary transcripts of *imp* and *syp* by intronic probes reveals that both RBPs are actively transcribed in iMNs and not only passively inherited from the NB (Figure S5). These results suggest that opposite gradients of Imp and Syp in iMNs result from their inheritance from the NB and their *de novo* transcription.

We next examined the function of Imp and Syp in shaping the correct connectome between Lin A/15 axons and leg muscles (Figure 5). Distal region of the tibia, which in wild-type (WT) Lin A/15 is innervated by last-born MNs expressing a low level of Imp during development, was not affected in *Imp*^{-/-} MARCM clones. By contrast, all the other regions were less innervated (Figures 5A, 5F, 5K, and S6; Table S2). In *Syp*^{-/-} MARCM clones, an opposite phenotype was observed. The distal region

Figure 3. TF expression is progressively shaped in iMNs during development

(A–C, E–G, I–K, and M–O) Plot of the relative position of each Lin A/15 cell from a lateral perspective (A1, B1, C1, E1, F1, G1, I1, J1, K1, M1, N1, and O1) and confocal sections (A2, A3, B2, B3, C2, C3, E2, E3, F2, F3, G2, G3, I2, I3, J2, J3, K2, K3, M2, M3, N2, N3, O2, and O3) showing the expression of Jim (A2, A3, B2, B3, C2, and C3), Oli (E2, E3, F2, F3, G2, and G3), Br (I2, I3, J2, J3, K2, and K3), and Chinmo (M2, M3, N2, N3, O2, and O3) (red) in GFP⁺ Lin A/15 (green) immunostained with anti-Dpn (cyan) and anti-Elav (blue) throughout development. Arrowheads indicate the NB. The developmental time points are indicated on top (EL3/ML3/LL3: early/mid/late L3). The expression patterns were evaluated at seven different time points with 2 to 3 CNS samples, and only representative time points were chosen for EL3/ML3/LL3. Boxed regions in (I3) and (K2) show the weak expression of Br in GFP-labeled cells. (A1, B1, C1, E1, F1, G1, I1, J1, K1, M1, N1, and O1) Left panel: Lin A/15 NB is in cyan, GMCs and proliferative glia (intermingled with MNs at early time points) are in white, iMNs are in blue, and the cells expressing a TF are in red. Right panel: only the TF-expressing cells are color coded in red. The black lines indicate the positions of the confocal sections of the lower panels. (D, H, L, and P) Schematic of the expression (red) of Jim (D), Oli (H), Br (L), and Chinmo (P) in Lin A/15 during larval stages. The TFs in the same categories are listed on top left of each schematic (see Figure S3 for all TF stainings).

of the tibia, innervated by last-born MNs expressing a high level of *Syp* during development, was no longer innervated by Lin A/15 axons, whereas other leg regions were correctly innervated. Interestingly, we observed more axonal branches than normal in the distal region of the femur in *Syp*^{-/-}, suggesting that abolishing *Syp* function is sufficient to re-direct axonal targeting from distal tibia to distal femur (Figures 5B, 5G, and 5K; Table S2). In *Syp*^{-/-} clones, more neurons are produced (Figure S6), probably due to the survival of the supernumerary and a late decommissioning of the NB as observed in *Syp RNAi* LinA/15 (Guan et al., 2021). The ectopic expression of *Imp* in all Lin A/15 cells, including the *Syp*⁺ cells (which normally express a low level of *Imp*), induced a similar innervation phenotype and an increase of the MN produced to that observed in *Syp*^{-/-} MARCM clones (Figures 5C, 5H, and 5K; Table S2). The result highlights the capacity of *Imp* to inhibit iMNs targeting into distal tibia and to promote the targeting of the distal femur. Only a minor innervation phenotype (the talm is not innervated) resulted from the overexpression of *Syp* in Lin A/15 (Figure S6), suggesting a dorsal prevalence of *Imp* over *Syp*. Although, *Imp* and *Syp* negatively cross-regulate each other in the brain and VNC NBs (Liu et al., 2015; Ren et al., 2017; Syed et al., 2017), *Imp* and *Syp* mutual inhibition was not observed in our genetic manipulations in late L3 VNC, indicating that both RBPs act independently on specifying axonal targeting (Figure S7).

In summary, our results show that *Syp* inhibits iMN targeting of the distal femur and promotes iMN targeting of distal tibia, whereas *Imp* has the opposite effect, with *Imp* required in early-born MNs for the correct targeting of the femur and proximal tibia. Finally, the strong increase in axonal branching of the distal femur in *Syp*^{-/-} and *Imp*-overexpressing Lin A/15 suggests that the surviving MNs are maybe integrated into the axon-muscle connectome.

Imp and Syp shape the LinA/15 TF codes

The function of *Imp* and *Syp* in shaping the axon-muscle connectome raised the question of whether they act through the post-transcriptional regulation of the TF codes. To address this

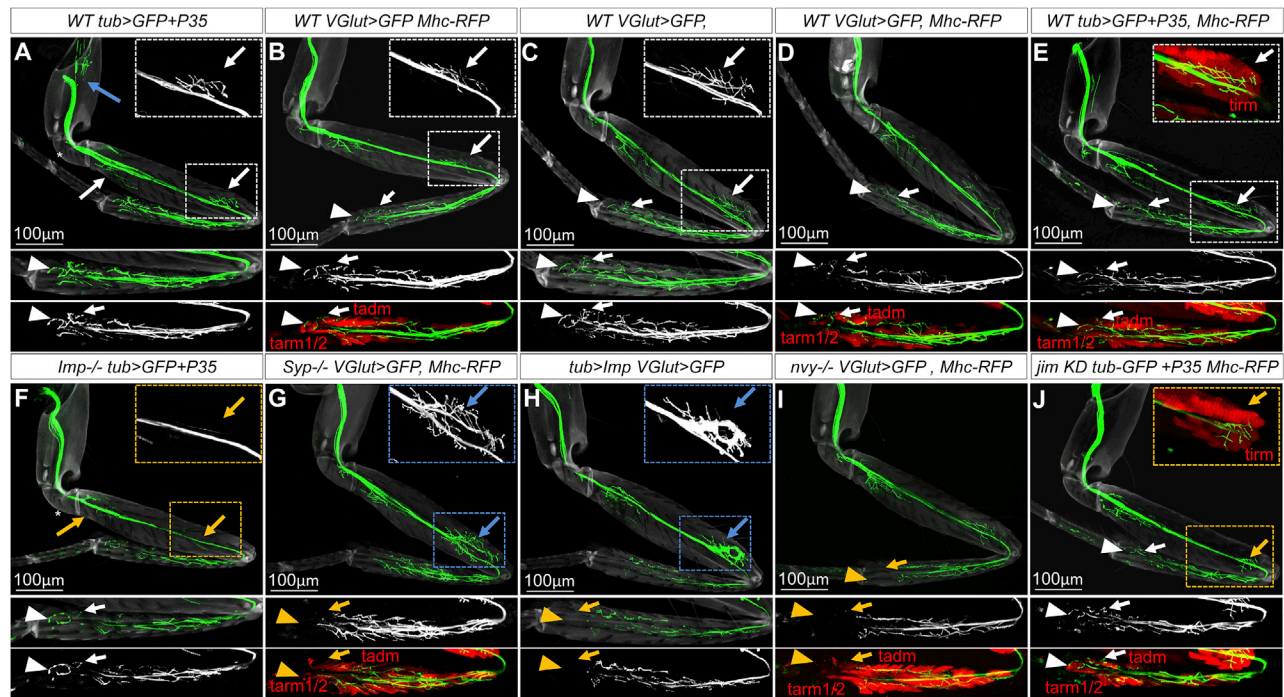
question, we focused on those six TFs whose expression has been characterized at the level of the RNA and protein—Mamo, Chinmo, Br, Nvy, Jim, and Oli (Figures 2 and 4)—and analyzed changes in their expression patterns when the levels of *Imp* and *Syp* were modified.

We tested the epistatic relationships between *Imp* and *Syp* and the TF codes in *Syp*^{-/-} and *Imp*-overexpressing Lin A/15 clones because both genetic backgrounds induced similar innervation phenotypes and were therefore anticipated to induce similar variations in TF expression. Br was expressed in fewer iMNs in the absence of *Syp* (Figures 6A, 6D, 6J, and 6Q), whereas it was unaffected by *Imp* overexpression (Figures 6A, 6G, 6M, and 6Q). Mamo expression was unaffected by the absence of *Syp*, but it was extended to more ventral iMNs with *Imp* overexpression (Figures 6C, 6F, 6I, 6L, 6O, and 6Q). The expression of Chinmo and Jim was extended to ventral iMNs, and Nvy was expressed in fewer iMNs with both the absence of *Syp* and the overexpression of *Imp* (Figures 6A, 6B, 6D, 6E, 6G, 6H, 6J, 6K, 6M, 6N, and 6Q). Interestingly, only the ventral cluster of *Nvy*⁺ iMNs (*Br*⁺) were affected by *Imp* overexpression, but not the dorsal cluster of *Nvy*⁺ iMNs (*Br*⁻) (Figures 6Q and S7). Oli expression was unaffected by both the absence of *Syp* and the overexpression of *Imp* (Figures 6Q and S7).

Finally, by using *VGlut*-Gal4 to label iMNs with GFP, we could observe some of the iMNs that are eliminated by apoptosis during later stages (*VGlut* > GFP did not label all of them because the driver is expressed with a delay in iMNs). However, the weak expression of the GFP in late-born iMNs and their ventral localization allowed us to recognize the iMNs that are eliminated by apoptosis in a later stage and to reveal that they express a code similar to MNs that targets the distal femur (*Jim*⁺, *Nvy*⁻ or low, *Br* low) in *Syp*^{-/-} and *Imp*-overexpressing Lin A/15 (Figures 6D1–6D4, 6E1–6E4, 6G1–6G4, and 6H1–6H4). These observations combined with the excessive amount of extra targeting into distal femur in *Syp*^{-/-} and *Imp*-overexpressing Lin A/15 (Figure 5) suggest that the surviving MNs are integrated in the axon-muscle connectome because their

Figure 4. Pattern of transcripts of indicated TFs and *Imp* and *Syp* proteins in Lin A/15

- (A) Lin A/15 labeled with *myr*:GFP (green).
 (B) Plots of the relative position of each Lin A/15 cell in (A) from lateral (top) and ventral (bottom) perspectives. Axes: M, medial. iMNs and GMCs are both in blue; NB is in cyan.
 (C) Confocal sections of the Lin A/15 in (A) labeled with DAPI (blue), *jim* mRNA (purple), and *Syp* mRNA (cyan). Note: *Syp* mRNAs are used to indicate the NB since it is highly abundant in NBs (boxed regions in C1). The boxed regions in (C1)–(C3) are enlarged at the top-right region of each panel, where the intensity of the GFP and smFISH signals was numerically enhanced in (C3) to highlight the dorsal weak signal due to the thickness of the tissue.
 (D) 3D segmented Lin A/15 cells of (A) (see STAR Methods). (Left) Lateral view is shown; (right) ventral view is shown. Each cell is color coded from low (blue) to high (red) based on the number of *jim* mRNA spots (spheres).
 (E) Plot of the expression level (E1) of the *jim* mRNA in Lin A/15 iMNs in (A) and plot of the average expression level (E2) of the *jim* mRNA in six Lin A/15 samples, as a function of their relative distance to the NB. Only the 29 iMNs most distant to NB are represented. See Table S1 for average number of *jim* mRNA spots from all samples analyzed.
 (F–I) (Top) Same graph as in (E2) for indicated TFs; $n \geq 4$ Lin A/15 samples (n , number of Lin A/15 samples analyzed) (see Figure S4 for *oli* mRNA expression). (Bottom left) 3D segmented Lin A/15 cells where *chinmo* (F), *mamo* (G), *br* (H), and *nvy* (I) mRNA are detected are shown. (Bottom right) One representative confocal section is shown. See Table S1 for average number of TF mRNA spots from all samples analyzed.
 (J) Confocal sections of a T2 Lin A/15 labeled with *myr*:GFP (green) and immunostained with anti-Jim (purple), anti-*Syp* (cyan), and anti-*Imp* (red). Boxed regions and arrowheads indicate the eight *Jim*⁺ iMNs.
 (K) Confocal section of a T2 Lin A/15 labeled with *myr*:GFP (green) and immunostained with anti-Dpn (purple), anti-*Syp* (cyan), and anti-*Imp* (red). The CNS was mounted laterally in (J1)–(K3).
 (L) Schematic of the expression of *Imp*, *Syp*, *Chinmo*, *Mamo*, *Jim*, *Br*, and *Nvy* proteins (horizontal bar, from Figure 2) and TF mRNAs (gradient) in LinA/15 iMNs (bottom).



K

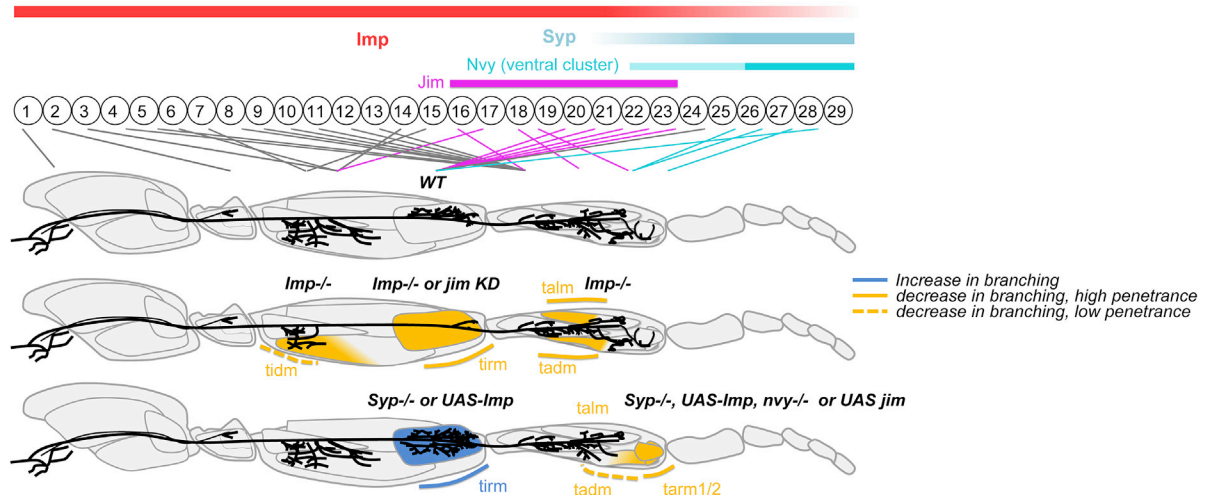


Figure 5. Function of *Imp*, *Syp*, and TF codes in building axonal-muscle connectome

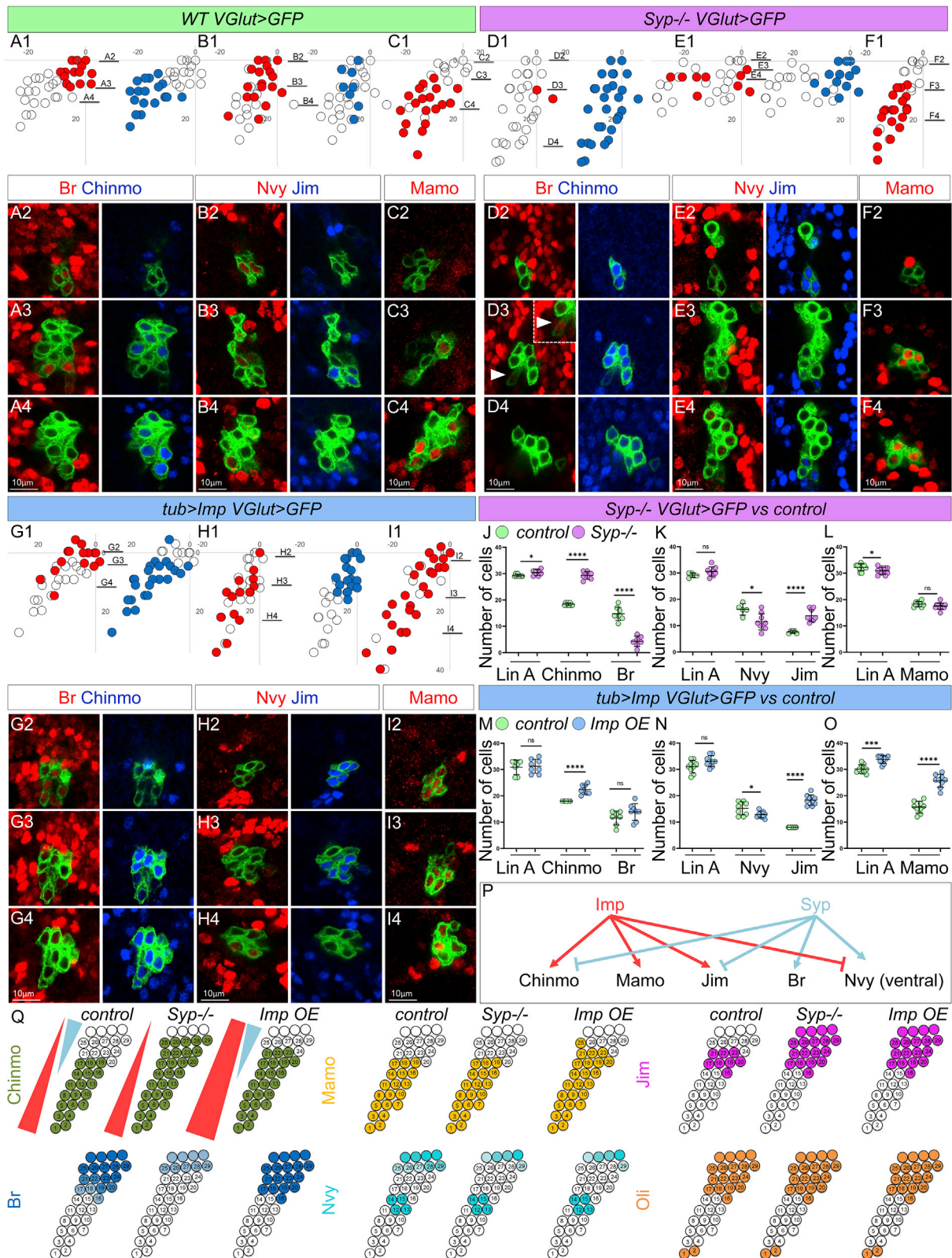
(A–J) Axonal targeting phenotypes of *WT tub > GFP+ P35* (A and E), *WT VGlut > GFP* (B–D), *Imp^{-/-} tub > P35* (F), *Syp^{-/-}* (G), *tub > Imp* (H), *nvyl^{-/-}* (I), and *jim KD* (J) *Lin A/15*. Axons are *mCD8:GFP⁺* (green); muscles were labeled with *Mhc-RFP* (red) in (B), (D), (E), (G), (I), and (J). Insets show leg regions most affected. Arrowheads and arrows point to normal targeting (white), the absence or reduction of targeting (orange), and extra targeting (blue). Asterisks indicate an absence of trochanter targeting in *Imp^{-/-} tub > P35* (F) that was not considered as part of the phenotypes because the *WT tub-P35* showed similar defects (A). In *WT tub > GFP+ P35 Lin A/15*, the supernumerary neurons targeted a new region in the coxa ($n = 8/9$). Note: for each indicated phenotype, a minimum of six legs are analyzed; see [Table S2](#) for details.

(K) Schematic of the axonal targeting phenotypes. See [Figure S6](#) for *Imp^{-/-}*, *br^{-/-}*, *chinmo^{-/-}*, and *Oli^{-/-}* phenotypes and the number of *Lin A/15* cells in each genetic background. See [Figure 7](#) for *UAS-Jim* phenotype. See [Table S2](#) for the penetrance.

fate is modified. In summary, *Imp* and *Syp* have opposite effects on the expression of several TFs: *Imp* promoted the expression of *Chinmo*, *Mamo*, and *Jim* proteins and inhibited the expression of *Nvy*, whereas *Syp* inhibited the expression of *Chinmo* and *Jim* and promoted the expression of *Br* and *Nvy* ([Figures 6P](#) and [6Q](#)).

TF code is functional in building the axon-muscle connectome

The opposite effects of *Imp* and *Syp* on TF expression could explain why *Syp^{-/-}* and *Imp*-overexpressing *Lin A/15* induced similar innervation phenotypes. To investigate such a possibility, we next analyzed the function of *Chinmo*, *Br*, *Nvy*, *Jim*, and



(legend on next page)

Oli in shaping the axon-muscle connectome (the attempts to analyze *mamo* were unsuccessful; Figure 5 and Figure S6).

Nvy is expressed in two different MN clusters. One of the clusters corresponds to the last-born MNs that mostly innervate the distal region of the tibia (Figure 2O). In *navy*^{-/-} clones, the distal region of the tibia is not or less innervated (Figures 5D, 5I, and 5K; Table S2). *Br* is expressed in MNs targeting the distal femur and distal tibia (Figure 2O). In *br*^{-/-} clones, the distal femur is less innervated, a phenotype associated with a mistargeting of the tilm (tibia levator muscle) (Figure S6; Table S2). In *jim* knockdown clones, the distal femur is less innervated by the four *Jim*-expressing iMNs that normally target this region (Figures 5E, 5J, and 5K; Table S2). In *chinmo*^{-/-} clones, both the proximal and distal regions of the femur were less innervated (Figure S6; Table S2). This axonal targeting defect at the distal femur, a region normally innervated by MNs never expressing *Chinmo*, suggests a non-autonomous function of *Chinmo* in these MNs (see discussion). The MNs expressing *Oli* are all affected with variable penetrance in *Oli*^{-/-} Lin A/15 MARCM clones (Figure S6; Table S2).

These phenotypes demonstrate that the TF code is functional in building the axon-muscle connectome.

Imp and Syp specify MN axonal targeting through reprogramming TF codes in iMNs

The phenotypic effects of *Imp*^{-/-}, *Syp*^{-/-}, or *Imp*-overexpressing (*UAS-Imp*) MARCM clones have more consistent effects on axon-muscle connectivity than removing a single TF (Figure 5 and Figure S6). The effects of *Imp* and *Syp* on axon-muscle connectivity are linked to the post-transcriptional regulation of multiple Lin A/15 TFs, thus explaining why removing one single TF cannot recapitulate the innervations phenotypes observed when levels of *Imp* and *Syp* are modified. However, some genetic manipulations modifying the level of TFs induced similar phenotypes to the ones generated in *Syp*^{-/-} or *Imp*-overexpressing Lin A/15. For example, *Nvy* and *Jim* are TFs necessary for specifying axonal targeting into distal tibia and distal femur respectively (Figures 5I–5K). In *Syp*^{-/-} or *Imp*-overexpressing Lin A/15, *Nvy* is repressed and *Jim* is ectopically translated in the iMNs that target distal tibia (Figures 6E, 6H, and 6Q), thus accordingly, the innervation in distal tibia is reduced and the axonal targeting at distal femur is increased (Figures 5G, 5H, and 5K).

In summary, the epistatic relationships of *Imp* and *Syp* with these TFs strongly imply that these RBP's shape the architecture of the axon-muscle connectome by shaping TF codes in iMNs.

Post-transcriptional regulation of TFs in iMNs by Imp shape the axon-muscle connectome

To establish the correct TF codes in iMNs, *Imp* and *Syp* could function in either the NB and/or iMNs. To discriminate between these two possibilities, we induced *Imp* expression in iMNs without affecting its temporal expression in the NB or GMC, using the *VGlut-Gal4* driver (Figure 7).

In this genetic background, muscle innervation phenotypes were similar to those generated by *Imp* overexpression in all Lin A/15 cells, including the NB (Figure 7B versus Figure 5H). In particular, the distal region of the tibia was not or was less innervated than normal. Moreover, similar epistatic relationships were observed between *Imp* and the TF codes to those observed by *Imp* overexpression in all Lin A/15 cells (Figures 7D–7J, *VGlut > Imp* versus Figures 6G–6I and 6M–6O, *tub > Imp*). In *VGlut > Imp* LinA/15, the number of iMNs expressing *Chinmo*, *Mamo*, *Jim*, and *Br* was higher, although the number of iMNs expressing *Nvy* was not statistically lower in *VGlut > Imp* MARCM clones (Figure 7J), while it was in *tub > Imp* MARCM clones (Figure 6N). Interestingly, the overexpression of *Jim* only in iMNs, including last-born MNs expressing a low level of *Imp* in WT, induces a similar phenotype as the one in *VGlut > Imp* LinA/15 and characterized by decreased innervation of the distal tibia (Figure 7C; Table S2).

These results show that the level of *Imp* shapes the axon muscle connectome through the regulation of TFs in iMNs. Together with above results, we propose a model where *Imp* and *Syp* shape the axon muscle connectome through the post-transcriptional regulation of TFs translation in iMNs (Figure 7K; see discussion).

DISCUSSION

Lin A/15 NB divides every 70 min (Baek and Mann, 2009), and at each division, it produces a GMC or intermediate mother cell (IMC) that generates an iMN with a unique developmental fate. Based on our results, we postulate that the LinA/15 NB divides too fast to implement neuronal identity using only transcriptional mechanisms to generate TF codes. The codes need time to be established in iMNs and thus depend on two layers of

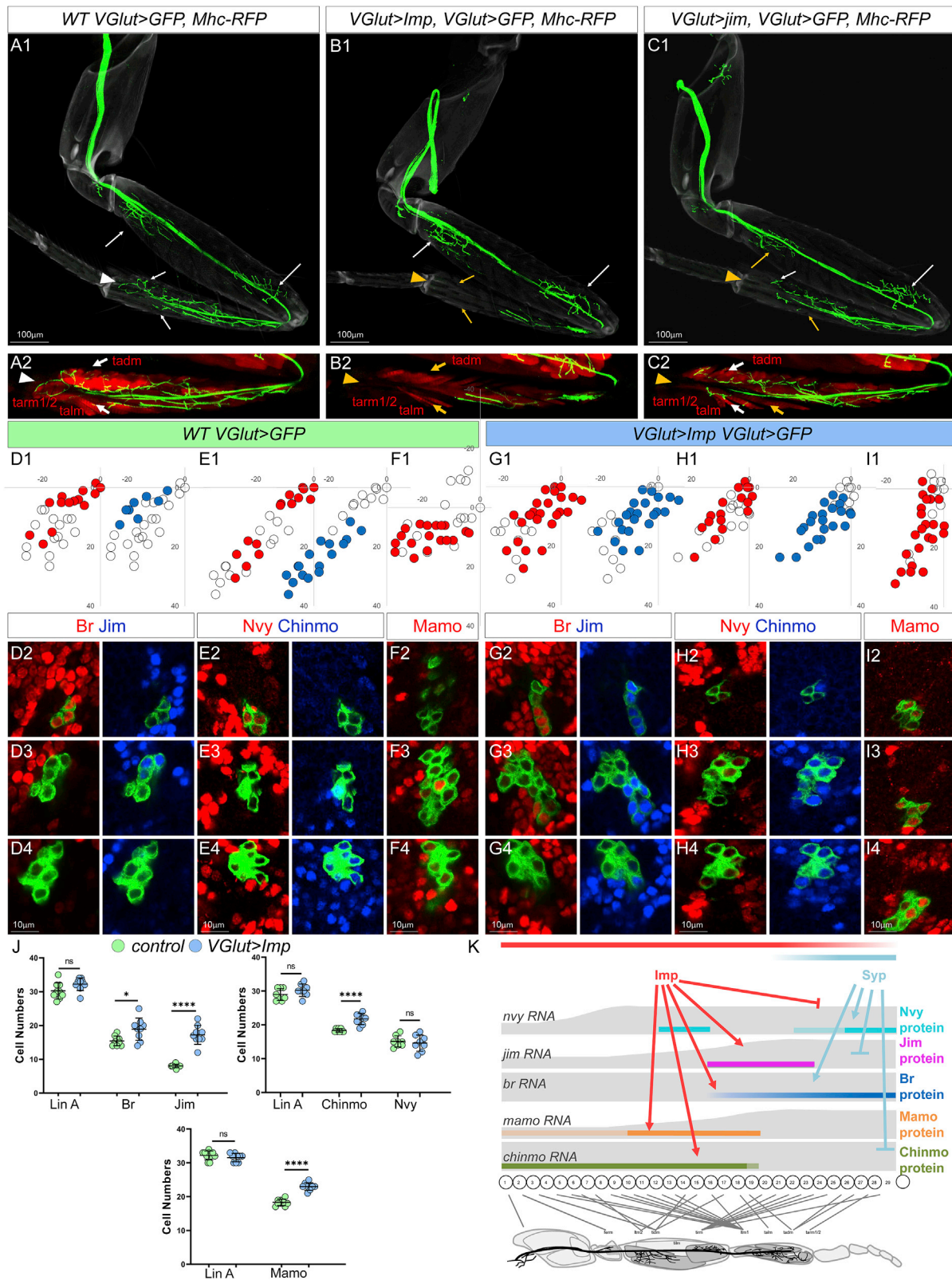
Figure 6. Opposite expression of Imp and Syp shapes the TF codes

(A–I) WT (A1–C4), *Syp*^{-/-} (D1–F4), and *tub > Imp* (G1–I4) Lin A/15 expressing mCD8:GFP (green) and immunolabeled with anti-*Br* (red) and anti-*Chinmo* (blue) (A1–A4, D1–D4, and G1–G4), anti-*Nvy* (red) and anti-*Jim* (blue) (B1–B4, E1–E4, and H1–H4), or anti-*Mamo* (red) (C1–C4, F1–F4, and I1–I4). (A1, B1, C1, D1, E1, F1, G1, H1, and I1) Plots of the relative position of each Lin A/15 cell from a lateral perspective are shown where cells expressing a given TF are color coded in red or blue according to the immunostaining in (A2)–(A4), (B2)–(B4), (C2)–(C4), (D2)–(D4), (E2)–(E4), (F2)–(F4), (G2)–(G4), (H2)–(H4), and (I2)–(I4), which are confocal sections from ventral to dorsal. Note: for each co-staining, a minimum of seven Lin A/15 samples are analyzed.

(J–O) Graph of the number of *VGlut*⁺ Lin A/15 iMNs expressing *Chinmo* (J and M), *Br* (J and M), *Nvy* (K and N), *Jim* (K and N), and *Mamo* (L and O) in *Syp*^{-/-} *VGlut > GFP* versus WT *VGlut > GFP* (J–L) and in *tub > Imp VGlut > GFP* versus WT *VGlut > GFP* (M–O). The number of Lin A/15 *VGlut*⁺ cells sometimes varied between controls or other genetic backgrounds due to the difficulty of having L3 larvae perfectly staged. However, the variations in (J) and (O) could not explain the large variation of the number of iMNs expressing *Chinmo*, *Br*, and *Mamo*. ns, not significant; differences of $p < 0.05$ were considered significant. * $0.01 < p < 0.05$; ** $0.001 < p < 0.01$; *** $0.0001 < p < 0.001$, **** $p < 0.0001$.

(P) Schematic of the epistasis between the Lin A/15 TFs and *Imp* and *Syp*.

(Q) Schematic of the expression pattern of *Chinmo*, *Mamo*, *Jim*, *Br*, *Nvy*, and *Oli* in WT, *Syp*^{-/-}, and *Imp* overexpression in an L3 Lin A/15. Note: only 33 iMNs are indicated because the readout was *VGlut > GFP*, which was expressed in around 30 iMNs at that stage (see Figure S7 for *Oli* expression).



(legend on next page)

regulation: the transcriptional expression of TF RNA and their post-transcriptional refinement. The transcriptional upstream regulators of the mRNAs coding for the TFs remain to be identified. In our system, Imp and Syp, which are known to control the temporal identity of NBs, are maintained as opposing gradients in iMNs according to their birth order. These opposite expression patterns are progressively decrypted into sharp mTF codes in iMNs, allowing for the generation of a large amount of neuronal diversity. Our study is a proof of concept that the temporal identity of the stem cell defined by two opposite gradients of RBPs can be deciphered by iMNs into TF codes. If we take into consideration the level of expression of the TF analyzed, our results reveal that both RBPs shape nine different TF codes. Below, we propose a model on how iMNs decode this temporal information.

From stem cells to immature neurons

This developmental logic regulating MNs targeting contrasts with mushroom body neurons. Lin A/15 NB produces few neurons with a high amount of morphological diversity, whereas the MB NBs generate a higher number of neurons with less morphological diversity. In Lin A/15, Imp and Syp are two key components of the post-transcriptional machinery shaping the TF codes, demonstrating that the post-transcriptional regulation of TFs is also compatible with lineages generating a large amount of neuronal diversity within a short period of time. Our results revealed that the differential sensitivities of TFs RNA to the relative concentrations of Imp and Syp explain how a gradient of two RBPs is transformed into unique TF codes. The molecular basis of these differential sensitivities could be found in the physical interaction between RNAs and RBPs since *jim*, *mamo*, *br*, and *pros* are known to immunoprecipitate with Imp and/or Syp (McDermott et al., 2014; Yang et al., 2017a). Investigating further into the mechanisms of Imp- and Syp-TF interaction by, for example, switching UTRs between TF RNAs, which are the regions interacting with RBPs, could help determine whether the range of proteins' expression is changed accordingly. Moreover, the expression gradient of some TF RNAs could also explain how two gradients of RBPs are decoded into sharp TF code. For example, *jim* RNA is expressed from low to high in iMN 1–iMN 29 and Jim protein might not be present in iMNs 1–15 because the threshold of *jim* RNA needed to have detectable protein is not reached. MNs 24–29 do not express Jim protein, even if *jim* RNA is highly expressed because of the inhibition of Jim transla-

tion by Syp. As a consequence, only the iMNs 16–23, expressing high level of *jim* RNA and Imp protein, expressed Jim protein.

Imp and Syp are multi-tasked proteins determining several facets of neuronal identity

Here, we have shown that Imp and Syp are important to determine one aspect of the MN identity, its morphology. However, both proteins might also determine other aspects of MN fate. In our parallel study, we have demonstrated that both RBPs act in iMNs to determine the survival of Lin A/15 MNs (Guan et al., 2021). Syp prevents the survival of iMNs, whereas Imp promotes it. Interestingly, both proteins might also control the biophysical identity of MNs. We were able to generate Lin A/15 *Imp*^{-/-} MARCM clones with a pan-cellular *tub-Gal4* driver, but not with *VGlut-Gal4*, an enhancer trap transgene of the gene coding for the vesicular glutamate transporter that is expressed by all *Drosophila* MNs (Mahr and Aberle, 2006). The TFs controlling these molecular features are called terminal selectors (Allan et al., 2005; Eade et al., 2012; Hobert, 2011, 2016). Good candidates for terminal selectors could be genes expressed in all iMNs, such as Lim 3 and Nkx6 found in our screen (Figure S1).

Muscle development is linked to innervation by MNs

The development of the locomotor system needs communication between different tissues, such as muscles and MNs. Muscle development was affected in several genetic backgrounds in addition to muscle innervation defects. The effect on muscle development is due to a non-autonomous effect of MNs on muscles because the genetic backgrounds only affected MNs. For example, in *nvy*^{-/-}, Jim-overexpressing, and Imp-overexpressing Lin A/15 clones, the *tarm1/2* is atrophic or absent when it was not innervated by LinA/15 axons (Figures 5 and 7). This dependence of muscle development on innervation by MNs might result from a lack of electrical activity or an absence of the neurotrophic factors secreted by MN axons. Another possibility could be that myogenesis is directly induced by innervation. Our work would stimulate further investigations on the dialogue between MN and muscles during development.

Limitations of the study

Even though our work emphasizes the role of Imp and Syp in iMNs, we could not exclude the possibility that both RBPs might also be important for the temporal identity of the NB, presumably through

Figure 7. Post-transcriptional regulations of TFs in iMNs by Imp shape the axon-muscle connectome

(A–C) Axon targeting phenotypes of *WT* (A1 and A2), *VGlut > Imp* (B1 and B2), and *VGlut > jim* (C1 and C2) Lin A/15 expressing mCD8:GFP (green). Muscles were labeled with *Mhc-RFP* (red). Arrowheads and arrows point to normal targeting (white) and the absence or reduced targeting (orange). Note: for each indicated phenotype, a minimum of 11 legs are analyzed; see Table S2 for the penetrance.

(D–I) *WT* (D1–F4) and *VGlut > Imp* (G1–I4) LinA/15 expressing *VGlut > mCD8:GFP* (green) and immunolabeled with anti-Br (red) and anti-Jim (blue) (D1–D4 and G1–G4), anti-Nvy (red) and anti-Chinmo (blue) (E1–E4 and H1–H4), or anti-Mamo (red) (F1–F4 and I1–I4). (D1, E1, F1, G1, H1, and I1) Plots of the relative position of each Lin A/15 cell from a lateral perspective, where cells expressing a given TF are color coded in red or blue according to the immunostaining in (D2)–(D4), (E2)–(E4), (F2)–(F4), (G2)–(G4), (H2)–(H4), and (I2)–(I4), which are confocal sections from ventral to dorsal; for each co-staining, a minimum of eight Lin A/15 samples are analyzed.

(J) Graph of the number of *VGlut*⁺ Lin A/15 MNs in *WT VGlut > GFP* versus *VGlut > Imp*, *VGlut > GFP* expressing Chinmo, Br, Nvy, Jim, and Mamo. Note: The increase of the number of iMNs expressing Br was also observed when affecting the level of Imp by using *tub > GAL4* driver, but the difference was not statistically significant (Figure 7J versus Figure 6M). ns, not significant; differences of $p < 0.05$ were considered significant. * $0.01 < p < 0.05$; ** $0.001 < p < 0.01$; *** $0.0001 < p < 0.001$, **** $p < 0.0001$.

(K) Schematic of a model explaining how the architecture of the axon-muscle connectome is shaped. The dotted and continuous lines indicate low and high expression levels of the TF proteins, respectively.

governing the expression of temporal TFs. *Chinmo*, a TF expressed in a limited time window in *Lin A/15* NB (Figure 3), serves as a putative downstream effector of *Imp* and *Syp* in specifying the temporal identity of *Lin A/15* NB. This could also explain the decrease in tirm innervation in *chinmo*^{-/-} *Lin A/15* clones that we interpret as a function of *Chinmo* in the NB (Figure S6).

Transcriptional upstream regulators inducing the expression of the TF RNA remain to be identified. We propose that spatial selectors expressed in a gradient manner could be the upstream regulators of TF mRNA expression, which are expressed ubiquitously as a gradient, such as *jim* or *mamo*. Candidates for spatial selectors could be the TFs found in our expression screen, such as *RunxB*, *Islet*, or *Jumu*, that have a gradient expression pattern in iMNs.

Finally, we cannot exclude that tTFs could function in parallel with RBPs to regulate mTF transcription, as has been shown in larval MNs (Seroka et al., 2020). Moreover, our results also show that not all mTFs, such as *Oli*, are sensitive to *Imp* and *Syp* concentration, suggesting that other post-transcriptional machinery remains to be identified.

STAR★METHODS

Detailed methods are provided in the online version of this paper and include the following:

- KEY RESOURCES TABLE
- RESOURCE AVAILABILITY
 - Lead contact
 - Materials availability
 - Data and code availability
- EXPERIMENTAL MODEL AND SUBJECT DETAILS
- METHOD DETAILS
 - Genetic Crosses for each figure
 - Lineage tracing and MARCM Clonal Analysis
 - Leg imaging
 - Immunostaining of larval CNS
 - Immunostaining of adult VNC
 - Primary and secondary antibodies
 - Image acquisition of immunostained VNC/CNS and adult legs
 - 5-Ethynyl-2′deoxyuridine (EdU) labelling
 - Probe design and preparation for smFISH
 - smFISH, sample preparation, and hybridization
 - Image acquisition of larval VNC after smFISH
 - smFISH analysis
 - Schematics
 - Cloning
 - MIMIC swap to generate *Mi{Trojan-VGluT-LexA::GAD.2}*
 - Positive Cell Cluster Detection (PCCD) method (Figure 2, see also PCCD note book in key resources table)
 - Test of the PCCD method by co-staining
 - *Lin A/15* MARCM clones vs *Lin A/15* memory system
 - Link between birth order and muscle targets: Corrections of (Baek and Mann, 2009)
- QUANTIFICATION AND STATISTICAL ANALYSIS

SUPPLEMENTAL INFORMATION

Supplemental information can be found online at <https://doi.org/10.1016/j.celrep.2022.110992>.

ACKNOWLEDGMENTS

We thank Alain Vincent, Filipe Pinto-Teixeira, and Steve Garvis for comments on the manuscript. This work was funded by the Atip-Avenir program, AFM (no. 21999), and FRM (no. AJE20170537445) to J.E.; the NIH: R01 NS070644 to R.S.M.; and the GWIS-Nell Mondy Trust and Elizabeth Weisburger Fellowships to L.V. We acknowledge the contribution of SFR Biosciences (Arthro-tool facility, UAR3444/CNRS, US8/INSERM, ENS de Lyon, UCBL) and of the IGFL facility platform.

AUTHOR CONTRIBUTIONS

Conceptualization, J.E., W.G., and L.V.; methodology, J.E., W.G., and L.V.; software, C.Godin. and J.E.; investigation, W.G., J.E., S.B., M.B., L.V., C.Guillermín., A.L., C.K., A.D., C.Godin., and S.U.; writing – original draft, J.E.; writing – review & editing, J.E., W.G., L.V., A.L., R.S.M., S.U., C.Guillermín., and M.B.; funding acquisition, J.E.; resources, J.E.; supervision, J.E. and W.G.

DECLARATION OF INTERESTS

The authors declare no competing interests.

Received: February 23, 2022

Revised: April 15, 2022

Accepted: June 1, 2022

Published: June 28, 2022

REFERENCES

- Allan, D.W., Park, D., St. Pierre, S.E., Taghert, P.H., and Thor, S. (2005). Regulators acting in combinatorial codes also act independently in single differentiating neurons. *Neuron* 45, 689–700. <https://doi.org/10.1016/j.neuron.2005.01.026>.
- Alsö, J.M., Tarchini, B., Cayouette, M., and Livesey, F.J. (2013). Ikaros promotes early-born neuronal fates in the cerebral cortex. *Proc. Natl. Acad. Sci. USA* 110, E716–E725. <https://doi.org/10.1073/pnas.1215707110>.
- Alyagor, I., Berkun, V., Keren-Shaul, H., Marmor-Kollet, N., David, E., Mayseless, O., Issman-Zecharya, N., Amit, I., and Schuldiner, O. (2018). Combining developmental and perturbation-seq uncovers transcriptional modules orchestrating neuronal remodeling. *Dev. Cell* 47, 38–52.e6. <https://doi.org/10.1016/j.devcel.2018.09.013>.
- Awasaki, T., Kao, C.-F., Lee, Y.-J., Yang, C.-P., Huang, Y., Pfeiffer, B.D., Luan, H., Jing, X., Huang, Y.-F., He, Y., et al. (2014). Making *Drosophila* lineage-restricted drivers via patterned recombination in neuroblasts. *Nat. Neurosci.* 17, 631–637. <https://doi.org/10.1038/nn.3654>.
- Baek, M., and Mann, R.S. (2009). Lineage and birth date specify motor neuron targeting and dendritic architecture in adult *Drosophila*. *J. Neurosci.* 29, 6904–6916. <https://doi.org/10.1523/JNEUROSCI.1585-09.2009>.
- Baek, M., Enriquez, J., and Mann, R.S. (2013). Dual role for Hox genes and Hox co-factors in conferring leg motoneuron survival and identity in *Drosophila*. *Dev. Camb. Engl.* 140, 2027–2038. <https://doi.org/10.1242/dev.090902>.
- Bayraktar, O.A., and Doe, C.Q. (2013). Combinatorial temporal patterning in progenitors expands neural diversity. *Nature* 498, 449–455. <https://doi.org/10.1038/nature12266>.
- Brierley, D.J., Blanc, E., Reddy, O.V., VijayRaghavan, K., and Williams, D.W. (2009). Dendritic targeting in the leg neuropil of *Drosophila*: the role of midline signalling molecules in generating a myotopic map. *PLoS Biol.* 7, e1000199. <https://doi.org/10.1371/journal.pbio.1000199>.

- Brierley, D.J., Rathore, K., VijayRaghavan, K., and Williams, D.W. (2012). Developmental origins and architecture of *Drosophila* leg motoneurons. *J. Comp. Neurol.* 520, 1629–1649. <https://doi.org/10.1002/cne.23003>.
- Broihier, H.T., and Skeath, J.B. (2002). *Drosophila* homeodomain protein dHb9 directs neuronal fate via crossrepressive and cell-nonautonomous mechanisms. *Neuron* 35, 39–50. [https://doi.org/10.1016/S0896-6273\(02\)00743-2](https://doi.org/10.1016/S0896-6273(02)00743-2).
- Broihier, H.T., Kuzin, A., Zhu, Y., Odenwald, W., and Skeath, J.B. (2004). *Drosophila* homeodomain protein Nkx6 coordinates motoneuron subtype identity and axonogenesis. *Development* 131, 5233–5242. <https://doi.org/10.1242/dev.01394>.
- Certel, S.J., and Thor, S. (2004). Specification of *Drosophila* motoneuron identity by the combinatorial action of POU and LIM-HD factors. *Development* 131, 5429–5439. <https://doi.org/10.1242/dev.01418>.
- Dasen, J.S., and Jessell, T.M. (2009). Chapter six Hox networks and the origins of motor neuron diversity. In *Current Topics in Developmental Biology* (Academic Press), pp. 169–200.
- Delile, J., Rayon, T., Melchionda, M., Edwards, A., Briscoe, J., Sagner, A., Klein, A., and Treutlein, B. (2019). Single cell transcriptomics reveals spatial and temporal dynamics of gene expression in the developing mouse spinal cord. *Development* 146. <https://doi.org/10.1242/dev.173807>.
- Dillard, C., Narbonne-Reveau, K., Foppolo, S., Lanet, E., and Maurange, C. (2018). Two distinct mechanisms silence chinmo in *Drosophila* neuroblasts and neuroepithelial cells to limit their self-renewal. *Development* 145, dev154534. <https://doi.org/10.1242/dev.154534>.
- Doe, C.Q., and Skeath, J.B. (1996). Neurogenesis in the insect central nervous system. *Curr. Opin. Neurobiol.* 6, 18–24. [https://doi.org/10.1016/s0959-4388\(96\)80004-3](https://doi.org/10.1016/s0959-4388(96)80004-3).
- Eade, K.T., Fancher, H.A., Ridyard, M.S., and Allan, D.W. (2012). Developmental transcriptional networks are required to maintain neuronal subtype identity in the mature nervous system. *PLoS Genet.* 8, e1002501. <https://doi.org/10.1371/journal.pgen.1002501>.
- Elliott, J., Jolicoeur, C., Ramamurthy, V., and Cayouette, M. (2008). Ikaros confers early temporal competence to mouse retinal progenitor cells. *Neuron* 60, 26–39. <https://doi.org/10.1016/j.neuron.2008.08.008>.
- Enriquez, J., Venkatasubramanian, L., Baek, M., Peterson, M., Aghayeva, U., and Mann, R.S. (2015). Specification of individual adult motor neuron morphologies by combinatorial transcription factor codes. *Neuron* 86, 955–970. <https://doi.org/10.1016/j.neuron.2015.04.011>.
- Enriquez, J., Rio, L.Q., Blazeski, R., Bellemin, S., Godement, P., Mason, C., and Mann, R.S. (2018). Differing strategies despite shared lineages of motor neurons and glia to achieve robust development of an adult neuropil in *Drosophila*. *Neuron* 97, 538–554.e5. <https://doi.org/10.1016/j.neuron.2018.01.007>.
- Fujioka, M., Lear, B.C., Landgraf, M., Yusibova, G.L., Zhou, J., Riley, K.M., Patel, N.H., and Jaynes, J.B. (2003). Even-skipped, acting as a repressor, regulates axonal projections in *Drosophila*. *Development* 130, 5385–5400. <https://doi.org/10.1242/dev.00770>.
- Garces, A., and Thor, S. (2006). Specification of *Drosophila* aCC motoneuron identity by a genetic cascade involving even-skipped, grain and zfh1. *Development* 133, 1445–1455. <https://doi.org/10.1242/dev.02321>.
- Guan, W., Venkatasubramanian, L., Baek, M., Mann, R.S., and Enriquez, J. (2018). Visualize *Drosophila* leg motor neuron axons through the adult cuticle. *J. Vis. Exp. JoVE*. <https://doi.org/10.3791/58365>.
- Guan, W., Bouchet, M., Darmas, A., and Enriquez, J. (2021). Shaping the size of a neuronal lineage: the role of Imp and Syp RBPs in the precise elimination of neurons by apoptosis. Preprint at bioRxiv. 2021.11.06.467542. <https://doi.org/10.1101/2021.11.06.467542>.
- Hobert, O. (2011). Regulation of terminal differentiation programs in the nervous system. *Annu. Rev. Cell Dev. Biol.* 27, 681–696. <https://doi.org/10.1146/annurev-cellbio-092910-154226>.
- Hobert, O. (2016). Terminal selectors of neuronal identity. *Curr. Top. Dev. Biol.* 116, 455–475. <https://doi.org/10.1016/bs.ctdb.2015.12.007>.
- Isshiki, T., Pearson, B., Holbrook, S., and Doe, C.Q. (2001). *Drosophila* neuroblasts sequentially express transcription factors which specify the temporal identity of their neuronal progeny. *Cell* 106, 511–521. [https://doi.org/10.1016/s0092-8674\(01\)00465-2](https://doi.org/10.1016/s0092-8674(01)00465-2).
- Jacob, J., Maurange, C., and Gould, A.P. (2008). Temporal control of neuronal diversity: common regulatory principles in insects and vertebrates? *Dev. Camb. Engl.* 135, 3481–3489. <https://doi.org/10.1242/dev.016931>.
- Kohwi, M., and Doe, C.Q. (2013). Temporal fate specification and neural progenitor competence during development. *Nat. Rev. Neurosci.* 14, 823–838. <https://doi.org/10.1038/nrn3618>.
- Konstantinides, N., Holguera, I., Rossi, A.M., Escobar, A., Dudragne, L., Chen, Y.-C., Tran, T., Jaimes, A.M., Özel, M.N., Simon, F., et al. (2022). A Complete Temporal Transcription Factor Series in the Fly Visual System. *Nature* 604 (Nature), pp. 316–322.
- Lacin, H., and Truman, J.W. (2016). Lineage mapping identifies molecular and architectural similarities between the larval and adult *Drosophila* central nervous system. *Elife* 5, e13399. <https://doi.org/10.7554/eLife.13399>.
- Landgraf, M., Roy, S., Prokop, A., VijayRaghavan, K., and Bate, M. (1999). Even-skipped determines the dorsal growth of motor axons in *Drosophila*. *Neuron* 22, 43–52. [https://doi.org/10.1016/S0896-6273\(00\)80677-7](https://doi.org/10.1016/S0896-6273(00)80677-7).
- Lee, T., and Luo, L. (1999). Mosaic analysis with a repressible cell marker for studies of gene function in neuronal morphogenesis. *Neuron* 22, 451–461. [https://doi.org/10.1016/S0896-6273\(00\)80701-1](https://doi.org/10.1016/S0896-6273(00)80701-1).
- Li, X., Chen, Z., and Desplan, C. (2013a). Temporal patterning of neural progenitors in *Drosophila*. *Curr. Top. Dev. Biol.* 105, 69–96. <https://doi.org/10.1016/B978-0-12-396968-2.00003-8>.
- Li, X., Erclik, T., Bertet, C., Chen, Z., Voutev, R., Venkatesh, S., Morante, J., Celik, A., and Desplan, C. (2013b). Temporal patterning of *Drosophila* medulla neuroblasts controls neural fates. *Nature* 498, 456–462. <https://doi.org/10.1038/nature12319>.
- Liu, Z., Yang, C.-P., Sugino, K., Fu, C.-C., Liu, L.-Y., Yao, X., Lee, L.P., and Lee, T. (2015). Opposing intrinsic temporal gradients guide neural stem cell production of varied neuronal fates. *Science* 350, 317–320. <https://doi.org/10.1126/science.aad1886>.
- Machado, S., Mercier, V., and Chiaruttini, N. (2019). LimeSeg: a coarse-grained lipid membrane simulation for 3D image segmentation. *BMC Bioinform.* 20, 2. <https://doi.org/10.1186/s12859-018-2471-0>.
- Mahr, A., and Aberle, H. (2006). The expression pattern of the *Drosophila* vesicular glutamate transporter: a marker protein for motoneurons and glutamatergic centers in the brain. *Gene Expr. Patterns* 6, 299–309. <https://doi.org/10.1016/j.modgep.2005.07.006>.
- Mattar, P., Ericson, J., Blackshaw, S., and Cayouette, M. (2015). A conserved regulatory logic controls temporal identity in mouse neural progenitors. *Neuron* 85, 497–504. <https://doi.org/10.1016/j.neuron.2014.12.052>.
- Maurange, C., Cheng, L., and Gould, A.P. (2008). Temporal transcription factors and their targets schedule the end of neural proliferation in *Drosophila*. *Cell* 133, 891–902. <https://doi.org/10.1016/j.cell.2008.03.034>.
- McDermott, S.M., Yang, L., Halstead, J.M., Hamilton, R.S., Meignin, C., and Davis, I. (2014). *Drosophila* Syncrip modulates the expression of mRNAs encoding key synaptic proteins required for morphology at the neuromuscular junction. *RNA* 20, 1593–1606. <https://doi.org/10.1261/ma.045849.114>.
- Okano, H., and Temple, S. (2009). Cell types to order: temporal specification of CNS stem cells. *Curr. Opin. Neurobiol.* 19, 112–119. <https://doi.org/10.1016/j.conb.2009.04.003>.
- Oyallon, J., Apitz, H., Miguel-Aliaga, I., Timofeev, K., Ferreira, L., and Salecker, I. (2012). Regulation of locomotion and motoneuron trajectory selection and targeting by the *Drosophila* homolog of Olig family transcription factors. *Dev. Biol.* 369, 261–276. <https://doi.org/10.1016/j.ydbio.2012.06.027>.
- Philippidou, P., and Dasen, J.S. (2013). Hox genes: choreographers in neural development, architects of circuit organization. *Neuron* 80, 12–34. <https://doi.org/10.1016/j.neuron.2013.09.020>.

- Prokop, A., and Technau, G.M. (1991). The origin of postembryonic neuroblasts in the ventral nerve cord of *Drosophila melanogaster*. *Dev. Camb. Engl.* *111*, 79–88. <https://doi.org/10.1242/dev.111.1.79>.
- Raj, A., van den Bogaard, P., Rifkin, S.A., van Oudenaarden, A., and Tyagi, S. (2008). Imaging individual mRNA molecules using multiple singly labeled probes. *Nat. Methods* *5*, 877–879. <https://doi.org/10.1038/nmeth.1253>.
- Ren, Q., Yang, C.-P., Liu, Z., Sugino, K., Mok, K., He, Y., Ito, M., Nern, A., Otsuna, H., and Lee, T. (2017). Stem cell-intrinsic, seven-up-triggered temporal factor gradients diversify intermediate neural progenitors. *Curr. Biol.* *27*, 1303–1313. <https://doi.org/10.1016/j.cub.2017.03.047>.
- Rueden, C.T., Schindelin, J., Hiner, M.C., DeZonia, B.E., Walter, A.E., Arena, E.T., and Eliceiri, K.W. (2017). ImageJ2: ImageJ for the next generation of scientific image data. *BMC Bioinf.* *18*, 529. <https://doi.org/10.1186/s12859-017-1934-z>.
- Sagner, A., and Briscoe, J. (2019). Establishing neuronal diversity in the spinal cord: a time and a place. *Development* *146*. <https://doi.org/10.1242/dev.182154>.
- Schindelin, J., Arganda-Carreras, I., Frise, E., Kaynig, V., Longair, M., Pietzsch, T., Preibisch, S., Rueden, C., Saalfeld, S., Schmid, B., et al. (2012). Fiji: an open-source platform for biological-image analysis. *Nat. Methods* *9*, 676–682. <https://doi.org/10.1038/nmeth.2019>.
- Schneider, C.A., Rasband, W.S., and Eliceiri, K.W. (2012). NIH Image to ImageJ: 25 years of image analysis. *Nat. Methods* *9*, 671–675. <https://doi.org/10.1038/nmeth.2089>.
- Seroka, A., Yazejian, R.M., Lai, S.-L., and Doe, C.Q. (2020). A novel temporal identity window generates alternating Eve+/Nkx6+ motor neuron subtypes in a single progenitor lineage. *Neural Dev.* *15*, 9–14. <https://doi.org/10.1186/s13064-020-00146-6>.
- Skeath, J.B., Wilson, B.A., Romero, S.E., Snee, M.J., Zhu, Y., and Lacin, H. (2017). The extracellular metalloprotease AdamTS-A anchors neural lineages in place within and preserves the architecture of the central nervous system. *Dev. Camb. Engl.* *144*, 3102–3113. <https://doi.org/10.1242/dev.145854>.
- Soler, C., Daczewska, M., Da Ponte, J.P., Dastugue, B., and Jagla, K. (2004). Coordinated development of muscles and tendons of the *Drosophila* leg. *Development* *131*, 6041–6051. <https://doi.org/10.1242/dev.01527>.
- Syed, M.H., Mark, B., and Doe, C.Q. (2017). Steroid hormone induction of temporal gene expression in *Drosophila* brain neuroblasts generates neuronal and glial diversity. *Elife* *6*, e26287. <https://doi.org/10.7554/eLife.26287>.
- Terman, J.R., and Kolodkin, A.L. (2004). Nery links protein kinase a to plexin-mediated semaphorin repulsion. *Science* *303*, 1204–1207. <https://doi.org/10.1126/science.1092121>.
- Thor, S., and Thomas, J.B. (1997). The *Drosophila* islet gene governs axon pathfinding and neurotransmitter identity. *Neuron* *18*, 397–409. [https://doi.org/10.1016/S0896-6273\(00\)81241-6](https://doi.org/10.1016/S0896-6273(00)81241-6).
- Thor, S., Andersson, S.G.E., Tomlinson, A., and Thomas, J.B. (1999). A LIM-homeodomain combinatorial code for motor-neuron pathway selection. *Nature* *397*, 76–80. <https://doi.org/10.1038/16275>.
- Truman, J.W., and Bate, M. (1988). Spatial and temporal patterns of neurogenesis in the central nervous system of *Drosophila melanogaster*. *Dev. Biol.* *125*, 145–157. [https://doi.org/10.1016/0012-1606\(88\)90067-x](https://doi.org/10.1016/0012-1606(88)90067-x).
- Tsanov, N., Samacoits, A., Chouaib, R., Traboulsi, A.-M., Gostan, T., Weber, C., Zimmer, C., Zibara, K., Walter, T., Peter, M., et al. (2016). smiFISH and FISH-quant – a flexible single RNA detection approach with super-resolution capability. *Nucleic Acids Res.* *44*, e165. <https://doi.org/10.1093/nar/gkw784>.
- Venkatasubramanian, L., Guo, Z., Xu, S., Tan, L., Xiao, Q., Nagarkar-Jaiswal, S., and Mann, R.S. (2019). Stereotyped terminal axon branching of leg motor neurons mediated by IgSF proteins DIP- α and Dpr10. *Elife* *8*, e42692. <https://doi.org/10.7554/eLife.42692>.
- Yang, C.-P., Samuels, T.J., Huang, Y., Yang, L., Ish-Horowicz, D., Davis, I., and Lee, T. (2017a). Imp and Syp RNA-binding proteins govern decommitment of *Drosophila* neural stem cells. *Development* *144*, 3454–3464. <https://doi.org/10.1242/dev.149500>.
- Yang, L., Titlow, J., Ennis, D., Smith, C., Mitchell, J., Young, F.L., Waddell, S., Ish-Horowicz, D., and Davis, I. (2017b). Single molecule fluorescence in situ hybridisation for quantitating post-transcriptional regulation in *Drosophila* brains. *Methods* *126*, 166–176. <https://doi.org/10.1016/j.ymeth.2017.06.025>.

STAR★METHODS

KEY RESOURCES TABLE

REAGENT or RESOURCE	SOURCE	IDENTIFIER
Antibodies		
rabbit anti-Castor	Gift from Claude Desplan	N/A
mouse anti Br-core	DSHB	Cat# 25E9.D7; RRID:AB_528104
guinea-pig anti-Jim	Gift from Claude Desplan	N/A
mouse anti-Prospero	DSHB	Cat#MR1A; RRID:AB_528440
guinea-pig anti-Runt	Gift from Kuniaki SAITO	N/A
rabbit anti-Nvy	Gift from Richard S. Mann	N/A
rabbit anti-RunXA	Gift from Claude Desplan	N/A
guinea-pig anti-FoxP	Gift from Chris Q Doe	N/A
guinea-pig anti-Lov	Gift from Claude Desplan	N/A
rabbit anti-Zfh1	Gift from Jim Skeath	N/A
guinea-pig anti-Kr	Gift from Claude Desplan	N/A
rat anti-Zfh2	Gift from Chris Q Doe	N/A
rabbit anti-Oli	Gift from Claude Desplan	N/A
rabbit anti-Mamo	Gift from Oren Schuldiner	RRID:AB_2665566
guinea-pig anti-Chinmo	Gift from Claude Desplan	N/A
rabbit anti-Eyeless	Gift from Claude Desplan	N/A
mouse anti-Elav	DSHB	Cat#9F8A9; RRID:AB_2314364
rat anti-Elav	DSHB	Cat#7E8A10; RRID:AB_528218
guinea-pig anti-Dpn	Gift from Jim Skeath (Skeath et al., 2017)	RRID:AB_2314299
rat anti-Imp	Gift from Claude Desplan	N/A
rabbit anti-Syp	Gift from Claude Desplan	N/A
goat anti-mouse Alexa 647	Invitrogen	Cat#A32728; RRID:AB_2633277
donkey anti-rat Alexa 647	Jackson	Cat#712-605-153; RRID:AB_2340694
goat anti-mouse Alexa 555	Invitrogen	Cat#A32727; RRID:AB_2633276
goat anti-rabbit Alexa 555	Invitrogen	Cat#A32732; RRID:AB_2633281
goat anti-Rat Alexa 555	Abcam	Cat#ab150166
donkey anti-guinea-pig DyLight405	Jackson	Cat#706-475-148; RRID:AB_2340470
Chemicals, peptides, and recombinant proteins		
Formaldehyde	Thermo Scientific	Cat#28908
PBS	Dutscher	Cat#X0515-500
Triton	Sigma	Cat#T8787-100mL
BSA	Sigma	Cat#A7906-500 g
Vectashield mounting medium	Vector Laboratories	Cat#H1000
Critical commercial assays		
Clicl-iT EdU imaging kit	Invitrogen	Cat#C10340
Experimental models: Organisms/strains		
UAD-KD (attP2[68A4])	(Awasaki et al., 2014)	N/A
dpn>KDRT-stop-KDRT>CRE (su(Hw)attP8 [8E10])	(Awasaki et al., 2014)	N/A
act>loxP-stop-loxP>LexA::P65 (attP40 [25C7])	(Lacin and Truman, 2016)	Tzumin Lee
lexAop-myr::GFP (su(Hw)attP5[50F1])	(Awasaki et al., 2014)	N/A
R10c12-GAL4 (3rd chromosome, attp2)	(Lacin and Truman, 2016)	N/A

(Continued on next page)

Continued

REAGENT or RESOURCE	SOURCE	IDENTIFIER
tubP-Gal4 (3rd chromosome,79A2)	Bloomington Drosophila Stock Center	BDSC: 5138
VGlut-GAL4 (2nd chromosome, 22E1)	Bloomington Drosophila Stock Center	BDSC: 26160
Mhc-RFP (2nd chromosome)	Bloomington Drosophila Stock Center	BDSC: 38464
VGlut-LexA::GAD (VGlutMI04979)	This study	N/A
UAS-P35 (2nd and 3rd chromosome)	Bloomington Drosophila Stock Center	BDSC: 5072; 5073
20XUAS-Imp-RM-FLAG (3rd chromosome)	(Liu et al., 2015)	N/A
UAS-RNAi jim (2nd chromosome, attp40)	Bloomington Drosophila Stock Center	BDSC: 42662
UAS-jim CDS (3rd chromosome, attp2)	This study	N/A
Syp ¹⁰³⁷⁵⁵ (3rd chromosome)	Harvard medical school, The Exelixis Collection	N/A
Imp ⁷ (X chromosome)	Gift from Florence Besse	N/A
nvy ^{PDFKG38} (2nd chromosome)	(Terman and Kolodkin, 2004)	N/A
br ^{nPr3} (X chromosome)	Bloomington Drosophila Stock Center	BDSC: 5964
Chinmo ^{CRISPRΔ1} (2nd chromosome)	(Alyagor et al., 2018)	N/A
Oli ^{A9} (2nd chromosome)	(Oyallon et al., 2012)	N/A
Recombinant DNA		
pJFRC165-20XUAS-IVS-R::PEST vector	Addgene	Cat#32142
pBS-KS-attB2-SA(2)-T2A-LexA::GADflw-Hsp70 vector	Addgene	Cat#78307
Software and algorithms		
Amira 3D software (version 6.2)	SCR_007353	https://www.fei.com/
ImageJ (version 1.48)	(Schneider et al., 2012)	https://imagej.nih.gov/ij/
ImageJ plugin Limeseg	(Machado et al., 2019)	https://imagej.net/LimeSeg
GraphPad (Prism 8)	SCR_002798	https://www.graphpad.com/scientific-software/prism/
MATLAB R2020	SCR_001622	http://www.mathworks.com/products/matlab/
PCCD note book	This study	Zenodo: https://doi.org/10.5281/zenodo.6576839
smFISH analysis source code	This study	Zenodo: https://doi.org/10.5281/zenodo.6576251

RESOURCE AVAILABILITY

Lead contact

Further information and requests for resources and reagents should be directed to and will be fulfilled by the lead contact, Jonathan Enriquez (jonathan.enriquez@ens-lyon.fr).

Materials availability

All fly stocks made in this study, as well as the nucleotide sequences of the plasmids used, are available from the [lead contact](#) without restriction.

Data and code availability

Microscopy data reported in this paper will be shared by the [lead contact](#) upon request. PCCD note book and smFISH analysis source code have been deposited at Zenodo and is publicly available as of the date of publication. DOIs are listed in the [key resources table](#). Any other additional information required to reanalyze the data reported in this paper is available from the [lead contact](#) upon request.

EXPERIMENTAL MODEL AND SUBJECT DETAILS

Experimental model for this study was the vinegar fly *Drosophila melanogaster*. A full list of strains used in the paper is included in the [Key resources table](#) and Genetic Crosses for each Figure. Unless otherwise described, flies were maintained on a standard cornmeal medium and kept at 25°C in a 12:12 h light:dark cycle. Males and females were chosen at random.

METHOD DETAILS

Genetic Crosses for each figure

Figures	Summary	Genetic crosses
Figures 1B and 1C Figures 1G–1K	WT (LinA/15 tracing labeling)	<i>R10c12-GAL4</i> TO <i>dpr>KDRT-stop-KDRT>CRE</i> ; <i>act>loxP-stop-loxP>LexA::P65, lexAop-</i> <i>myr::GFP; UAS-KD</i>
Figure 1D	WT (LinA/15 MARCM Clone)	<i>y,w, hs-Flp^{1.22}; VGlut-Gal4,</i> <i>UASmCD8::GFP, Mhc-RFP, FRT42D/CyO;</i> <i>TM6B/MKRS</i> TO <i>y,w, hs-Flp^{1.22}; VGlut-Gal4, UAS-</i> <i>mCD8::GFP, Mhc-RFP, FRT42D, tubP-</i> <i>Gal80/CyO; MKRS/TM6B</i>
Figures 2B–2G Figure 2N Figure 3 Figures 4A–4C Figures 4J and 4K	WT(LinA/15 tracing labeling)	<i>R10c12-GAL4</i> TO <i>dpr>KDRT-stop-KDRT>CRE</i> ; <i>act>loxP-stop-loxP>LexA::P65, lexAop-</i> <i>myr::GFP; UAS-KD</i>
Figure 5B Figure 5G Figures 6A–6C Figures 6D–6F	WT and <i>Syp</i> ^{-/-}	<i>y,w, hs-Flp^{1.22}; VGlut-Gal4, UAS-</i> <i>mCD8::GFP, Mhc-RFP; FRT82B, tubP-</i> <i>Gal80/TM6B</i> TO <i>y,w, hs-Flp^{1.22}; VGlut-Gal4, UAS-</i> <i>mCD8::GFP, Mhc-RFP/CyO; FRT82B/</i> <i>TM6B</i> for Figures 5B and 6A–6C TO <i>y,w, hs-Flp^{1.22}; DVGlut-Gal4, UAS-</i> <i>mCD8::GFP, Mhc-RFP/CyO; FRT82B,</i> <i>Syp⁶⁰³⁷⁵⁵/TM6B</i> for Figures 5G and 6D–6F
Figure 5C Figure 5H Figures 6G–6I	WT and <i>tub</i> ^{>imp}	<i>y,w, hs-Flp^{1.22}; VGlut-</i> <i>LexA::GAD, 13XLexAop-mCD8GFP,</i> <i>FRT42D/CyO; tubP-GalGAL4/TM6B</i> TO <i>y,w, hs-Flp^{1.22}; FRT42D, tubP-Gal80/</i> <i>CyO; MKRS/TM6B</i> for Figure 5C TO <i>y,w, hs-Flp^{1.22}; FRT42D, tubP-Gal80/</i> <i>CyO; 20XUAS-Imp-RM-FLAG/TM6B</i> for Figures 5H and 6G–6I
Figure 5A Figure 5F	WT and <i>Imp</i> ^{-/-}	<i>y,w, hs-Flp^{1.22}, tubP-Gal80, FRT19A; UAS-</i> <i>P35/CyO; tubP-GAL4, QUAS-mCD8::GFP/</i> <i>TM2</i> TO <i>y, w, hs-Flp^{1.22}, FRT19A/FM7; VGlut-</i> <i>Gal4, UAS-myr::GFP</i> for Figure 5A TO <i>Imp⁷, FRT19A/FM7; VGlut-GAL4, UAS-</i> <i>myr::GFP/CyO</i> for Figure 5F
Figure 5D Figure 5I	WT and <i>nvy</i> ^{-/-}	<i>y,w, hs-Flp^{1.22}; VGlut-GAL4, UAS-</i> <i>mCD8::GFP, Mhc-RFP, FRT42D, tubP-</i> <i>GAL80/CyO; UAS-mCD8::GFP/MKRS</i> TO <i>hs-Flp^{1.22}, UAS-mCD8::GFP; VGlut-</i> <i>Gal4, FRT42D/CyO; UAS-mCD8::GFP/</i> <i>MKRS</i> for Figure 5D TO <i>hs-Flp^{1.22}, UAS-mCD8::GFP; VGlut-</i> <i>Gal4, FRT42D, nvy^{PDFKG38}/CyO; UAS-</i> <i>mCD8::GFP/MKRS</i> for Figure 5I

(Continued on next page)

Continued

Figures	Summary	Genetic crosses
Figure 5E Figure 5J	WT-P35 and jim KD-P35	<i>y,w, hs-Flp^{1,22}; VGlut-Gal4, UAS-mCD8::GFP, Mhc-RFP, FRT42D/CyO; tubP-Gal4/MKRS</i> <i>TO y,w, hs-Flp^{1,22}; FRT42D, tubP-Gal80/CyO; UAS-P35/TM6B</i> for Figure 5E <i>TO y,w, hs-Flp^{1,22}; UAS-RNAi jim, FRT42D, tubP-Gal80/CyO; UAS-P35/TM6B</i> for Figure 5J
Figures 7A–7C Figures 7D–7I	WT and VGlut>Imp and VGlut>Jim	<i>y,w, hs-Flp^{1,22}; VGlut-Gal4, UAS-mCD8::GFP, Mhc-RFP FRT42D/CyO; TM6B/MKRS</i> <i>TO y,w, hs-Flp^{1,22}; VGlut-Gal4, UAS-mCD8::GFP, Mhc-RFP, FRT42D, tubP-Gal80/CyO; MKRS/TM6B</i> for Figures 7A and 7D–7F <i>TO y,w, hs-Flp^{1,22}; VGlut-Gal4, UAS-mCD8::GFP, Mhc-RFP, FRT42D, tubP-Gal80 /CyO ; 20XUAS-Imp-RM-FLAG /TM6B</i> for Figures 7B and 7G–7I <i>TO y,w, hs-Flp^{1,22}; VGlut-Gal4, UAS-mCD8::GFP, Mhc-RFP, FRT42D, tubP-Gal80/CyO; UAS-jim /TM6B</i> for Figure 7C

Lineage tracing and MARCM Clonal Analysis

LinA/15 tracing labeling is achieved by immortalizing Gal4 expression in Lin A/15 neuroblasts and its descendants (Awasaki et al., 2014; Lacin and Truman, 2016). Fly strains used to specifically label LinA/15 are listed in *Genetic crosses for each figure*.

All fly strains used to introduce MARCM (Lee and Luo, 1999) clones labeling LinA/15 are listed in *Genetic Crosses for each Figure*. To introduce MARCM clones, embryos were collected for 12hs in vials and incubated for 24hs at 25°C. First-instar larvae (0~12h ALH) were heat shocked at 37°C for 20 min to induce mosaic clones in L3 larvae and at 35°C for 15min to induce mosaic clones in adults. All flies were then raised at 25°C degrees at the exception of *Imp -/- tub>GFP+P35* flies being raised at 29°C after heat shock to boost the efficiency of P35 (Figure 5F). P35 is added in the genetic background only when less MNs are produced in a given genetic perturbation, it is a way to exclude the possibility that the axonal targeting defect is the result of less MNs produced. In terms of the GAL4 driver (*tub* vs *VGlut*), the reason for choosing *tub* instead of *VGlut* are as follows: Figures 5F and S6: *Imp -/- tub>GFP: VGlut>GFP* failed to label LinA MNs: our hypothesis is that *Imp* is necessary for *VGlut* expression; Figure 5J: *jim KD tub>GFP*: a better knocking down efficiency is observed for *RNAi-jim* using *tub* driver compared to *VGlut* driver, probably due to the delayed onset of *VGlut* in MNs compared to *tub*. Figure S6: *chinmo -/-, tub>GFP*: *chinmo -/-* MARCM clones was impossible to generate with *VGlut* because of the proximity of genomic localization between *chinmo* (Chr2L, 22A) and *VGlut* (Chr2L, 22E) that make recombination events very rare, and thus the chromosome carrying both elements nearly impossible to recover.

Leg imaging

Legs were dissected, fixed, and imaged as described in (Guan et al., 2018).

Immunostaining of larval CNS

Inverted L3 larvae were fixed in 4% paraformaldehyde in PBS for 20 min at room temperature and blocked in the blocking buffer for one hour. L3 larval or pupal CNS were carefully dissected in PBS and then incubated with primary antibodies overnight (≥ 12 h) and secondary antibodies in dark for one day (≥ 12 h) at 4°C. Fresh PBST-BSA (PBS with 0.3% Triton X-100, 1% BSA) was used for the blocking, incubation, and washing steps: five times for 20 min at room temperature after fixation and after primary/secondary antibodies. Larval/pupal CNS were mounted onto glass slides using Vectashield anti-fade mounting medium (Vector Labs). Slides were either imaged immediately or stored at 4°C.

Immunostaining of adult VNC

After removing the abdominal and head segments, the thorax of the flies was opened and fixed in 4% paraformaldehyde in PBS for 25 min at room temperature and blocked in the blocking buffer for 1 h. After dissection, adult VNC was incubated with primary antibodies for 1 day and secondary antibodies in dark for 1 day at 4°C. Fresh PBST-BSA (PBS with 0.3% Triton X-100, 1% BSA) was used for the blocking, incubation, and washing steps: five times for 20 min at room temperature after fixation and after

primary/secondary antibodies. VNC was mounted onto glass slides using Vectashield anti-fade mounting medium (Vector Labs). Slides were either imaged immediately or stored at 4°C.

Primary and secondary antibodies

We screened around 220 antibodies against transcription factors (at least 10 CNSs/TF) from various sources including: a collection of antibodies generated by the modENCODE provided to us by C. Desplan (Li et al., 2013a); Developmental Studies Hybridoma Bank and various gifts from the Drosophila community. Antibodies used for the 16 TFs (expressing in different clusters of Lin A/15 MNs) are listed in [key resources table](#). Other TFs screened are following: Grh, Insv, Vvl, E93, Lim3, Nkx6, RunXB, Antp, Islet, Jumu, Gt, Psq, Seq, Ind; Adf1, E2F1, E2F2, Zelda, Sd, Snr1, Inv, ham, Hth, Tll, Grn, Ato, CG8108, CG12391, Dalao, Br-Z1, Br-Z3, vestigial, twist, gooseberry, gooseberry neuro, POU domain protein 2, salr, rotund, mad, labial, deformed, midline, vrlle, even skipped, achaete-c, knot, ladybird early, eagle, sloppy paired 1, Dichaete, apontic, LIM homeobox 1, extra-extra, Escargot, dachshund, period, Grain II, SVP, Hb9, Toy, Eg, En, Grn, Hkb, Msh, Nub, Eya, common spalt domain, klumpfuss, pointed, cryptocephal, Sox15, knirps, sloppy paired 2, Huckebein, Lim1, pdm1, acj6, abrupt, anterior open, apterous, bicoid, brain-specific homeobox, caudal, cut, defective proventriculus, empty spiracles, engrailed, extradenticle, eyegone, eyes absent, fushi tarazu, pebbled, intermediate neuroblasts defective, odd paired, odd skipped, Optix, paired, Ptx1, Retinal Homeobox, senseless, Sex combs reduced, so, snail, spineless, teashirt, Vsx1, Vsx2, Zelda, BarH1, CG3065, CG3281, CG7963, CG8478, cropped, CTCF, D1, Dorsocross2, Drop, Dsp1, eIB, Fer3, GATAe, Hnf4, Hr39, Jra, l(1) sc, pho, phol, Smox, Sox21a, Sox21b, SoxN, srp, sug, Taf12, tin, zeste, abdominal A, cubitus interruptus, crocodile, disco, deformed wings, fussel, Meics, ocelliless, p53, pangolin, pita, stat92E, stc, Suppressor of Hairless, Trithorax-like, wdn, wor, tramtrack, Ubx, Medea, cap-n-collar, Dpn, Repo, Pb, Dll, abdominal B, forkhead, buttonhead, CG11617, CG4360, D19a, BtbVII, Blimp-1, CG18619, Ods-site homeobox, Eip75B, HMG protein Z, maf-S, lozenge, Tj, Mef2, myc, mod(mdg4), Scr, cubitus interruptus, extradenticle, lola like, Trithorax-like, tramtrack, ash2, BEAF-32, Bgb, Bro, CG1832, CG3075, E(bx), E(z), knirps-like, Polycomblike, Rel, dwg, ftz-f1, hunchback.

Image acquisition of immunostained VNC/CNS and adult legs

Multiple 0.5- μ m-thick and 1- μ m-thick sections in the z axis for larval/pupal CNS or adult VNC and adult legs respectively were imaged with a Leica TCS SP8 or a Zeiss LSM 780 confocal microscope. Objective used: 40 \times /1.3 oil objective for larval/pupal CNS or adult VNC; 20 \times glycerol objective for adult leg samples. Binary images for z stack images were generated using NIH ImageJ.

5-Ethynyl-2'-deoxyuridine (EdU) labelling

To mark MNs born at different time points (Figures 1I–1K), L2 or L3 larvae (48, 72 and 96 h after egg laying [AEL]) were transferred from standard fly food to fly food containing 250 mM EdU. Larvae were dissected at 120 h AEL and dissected CNS were fixed in 4% paraformaldehyde in PBS for 20 min at room temperature, followed by a quick wash with PBST (PBS with 0.3% Triton X-100). EdU labeling was then detected using Click-iT EdU imaging kit (Invitrogen) according to manufacturer's instructions. An immunostaining was then performed as described in the Immunostaining section.

Probe design and preparation for smiFISH

Primary probes against mRNA sequences of genes of interest (common sequence of all isoforms of genes of interest; up to 48 probes per gene) were designed using the Biosearch Technologies stellaris RNA FISH probe designer tool (free with registration, <https://biosearchtech.com>). The probe sequences for each gene used in this study have been deposited at Zenodo (Zenodo: <https://doi.org/10.5281/zenodo.6592760>) and is publicly available as of the date of publication. The following sequence was added to the 5' end of each 20 nucleotide (nt) probe: CCTCCTAAGTTTCGAGCTGGACTCAGTG, which is the reverse complement of the X flap sequence (CACTGAGTCCAGCTCGAACTTAGGAGG) used in (Tsanov et al., 2016). The 5'-extended primary probe sets were synthesized by Integrated DNA Technologies (IDT), using 25 nmole synthesis scale, standard desalting, and at 100 μ M in nuclease-free H₂O. The X flap sequence, 5' and -3' end-labeled with Quasar 570, is synthesized by Biosearch Technologies. Fluorophore-labeled probe sets are prepared as described in (Tsanov et al., 2016), by hybridizing the fluorophore-labeled X Flap sequence and 5'-extended primary probe sets.

smiFISH, sample preparation, and hybridization

Dissected larval CNS from third instar larvae were fixed in 4% paraformaldehyde (in PBS with 0.3% Triton X-100) for 20 minutes at room temperature. Samples were washed for 3 times of 15 min with PBST (PBS with 0.3% Tween-20) before a pre-hybridization wash in smiFISH wash buffer (10% deionised formamide (stored at -80° C) and 2X SSC in DEPC water) at 37°C for 30 min. Samples were then incubated with hybridized fluorophore-labeled probe sets diluted in smiFISH hybridization buffer (10% deionized formamide, 2x SSC and 5% dextran sulphate in DEPC water) at 37°C for 12 to 14 h. The working concentration of each probe sets are: jim (400 nM), chinmo (800 nM), br (1 μ M), nvy (2 μ M), mammo (2 μ M) and oli (400 nM). Samples were washed for 40 min at 37°C followed by three times of 15 min in smiFISH wash buffer at room temperature, and 10 min of washing in PBST (PBS with 0.3% Tween 20) before sample mounting. Protocol adapted from (Yang et al., 2017b).

Image acquisition of larval VNC after smFISH

Images were acquired on a Leica TCS SP8 microscope using a 40x/1.3 oil objective. Image stacks were taken with the following settings: format 4400x4400 (223,56 μm * 223,56 μm (XY) and 44,95 μm (Z)), speed 700 Hz, unidirectional, sequential line scanning, line averaging 8, pinhole 1 airy unit. Image stacks were acquired with a 350 nm z interval. Parameters for the three channels used in this study are: DAPI excitation 405 nm, laser 2%, detection 412–496nm; GFP excitation 488nm, laser 4.5%, detection 494–530nm; Quasar 570 excitation 548nm, laser power 5%, detection 555–605nm.

smFISH analysis

See also smFISH analysis source code in the [Key resources table](#). Each Lin A/15 cell was segmented in 3D in ImageJ/Fiji (Rueden et al., 2017; Schindelin et al., 2012; Schneider et al., 2012), using the LimeSeg plugin (Machado et al., 2019), on the GFP channel, with the following parameters: D₀~4–6, F pressure = 0.01, Z_{scale} = 6.8, Range in d0 units~4–6, Number of integration step = -1, real XY pixel size = 50. For subsequent analysis, each segmented cell was exported into a separate ply file which was then imported in MATLAB as a point cloud (The Math Works, Inc.). The original stacks were imported in Matlab using the Bio-Formats toolbox (<https://www.openmicroscopy.org/bio-formats/downloads/>). These stacks were then cropped around each cell using the point clouds generated by individual cell segmentation with LimeSeg.

The mRNA spots were detected in 3D, in the mRNA channel of these cropped stacks, using the method described by (Raj et al., 2008). In short, the spots were identified computationally by running a Matlab image processing script that runs the raw data through a filter (Laplacian of a Gaussian) designed to enhance spots of the correct size and shape while removing the slowly varying background. The filtered stacks are then thresholded to disregard remaining background noise. In order to choose an optimal threshold, all possible thresholds are computed. The thresholds were always chosen manually and close to the plateau. A ‘check File stack’ for each cell was generated in order to visualize the accuracy of the spot detection for a given threshold. In most of our samples, common thresholds were chosen for all the cells of a given Lin A/15. However, specific thresholds were occasionally chosen for some cells. The parameters that gave the best visual detection of mRNA spots in our datasets-check files were generated were as follow: width of the Gaussian filter = 5; variance of the Gaussian filter = 0.25; threshold = 0.11 for *jim*, 0.08 for *chinmo*, 0.15 for *mamo*, 0.09 for *br*, 0.29 for *nvy* and 0.15 for *oli*. The detected spots in each cell had a normal distribution of diameters with a mean of 0.25 +/- 0.05 micrometers and their maximum intensities displayed a unimodal distribution, arguing that the detected spots are mostly individual molecules. A custom Matlab routine transformed the point clouds corresponding to segmented cell volumes obtained from the LimeSeg plugin into an alpha shape (critical radius = 100) and then returned the number of mRNA contained in this cell volume using the Matlab function inShape.

Schematics

All schematics were done with Microsoft PowerPoint.

Cloning

Pattb-20XUAS-hsp70-Jim-sv40. The full coding sequence of *jim* (2469bp) where the XhoI site in exon 1 was mutated to CTCCAG was ordered from Genewiz and cloned (XhoI/XbaI fragment) in the plasmid pJFRC165-20XUAS-IVS-R::PEST (<https://www.addgene.org/32142/>). The resulting *Pattb-20XUAS-hsp70-jim-sv40* construct was inserted in position 86f on chromosome III by injection into embryos carrying *attP-86f* landing site.

MIMIC swap to generate Mi{Trojan-VGlut-LexA::GAD.2}

The plasmid *pBS-KS-attB2-SA(2)-T2A-LexA::GADfluv-Hsp70* was ordered from Addgene (<https://www.addgene.org/78307/>) and inserted in the MiMIC Mi{MIC}VGlut[MI04979] (BDSC_38078) line inserted into the relevant intron in Phase 2 of the *VGlut* gene.

Positive Cell Cluster Detection (PCCD) method (Figure 2, see also PCCD note book in key resources table)

The Positive Cell Cluster Detection (PCCD) method aims to link the expression of a given TF to the birth-order of an immature MN (iMN) by using the correlation between the birth-order of iMNs and their spatial organization. In our Lin A/15 model, the EdU experiments (Figure 1) reveal a good correlation between the birth order of iMNs and their spatial distance from the NB in 3rd instar larvae: young born iMNs are farther away from the NB compared to older iMNs. The final goal of this method is to predict the TF code expression pattern in each iMNs in a third instar larva.

The method followed a series of steps

Step 1: From the imaging, assign spatial x, y, z coordinates and the expression (on/off) of a given TF to each Lin A/15 cell (N > 15, Number of Lin A/15 immunostained for a given TF).

Step 2: Calculate the Euclidean distance between the NB and the x, y, z, coordinates of each iMN (relative distance).

Step 3: Order iMNs in each Lin A/15 according to their distance to NB. This presents each Lin A/15 as an ordered sequence of iMNs (this defines the x axis position where cell #1 is defined as the furthest from the NB, i.e. the oldest iMNs on average). Then calculate the frequency of expression of all TFs as a function of their rank in each ordered Lin A sequence.

Step 4: Apply a filter (Savitzky-Golay) to smooth each distribution.

Step 5: Define the position in the sequence of the positive cell cluster(s) by using a peak detection method. Determine its length (average number of cells expressing a given TF in all Lin A/15 samples analyzed). Then find the position of the positive cell cluster with this average length compatible with the smoothed TF distribution. The position and its length are represented by a horizontal line.

Step 6: Assemble all positive cell clusters for each TF on the same graph to reveal combinatorial TF code for each iMN. Convert the x' axis to a birth order axis (1–29) since the distance between iMN and the NB is tightly linked to their birth order. Define the coverage index at the border of all cell clusters.

More details about the method include

Savitzky-Golay filter (Step 4): The Savitzky-Golay algorithm (polynomial filter) was set with a window of size 11 and a polynomial order of 3 (see `scipy.signal.savgol_filter` function from the `scipy` python library).

Peak detection method (Step 5): Peaks were detected as local maxima in the normalized TF distributions. Local maxima were determined according to local conditions. They had a minimal height ($h_{\min} = 0.02$), a minimal distance from other peaks ($d_{\min} = 15$), and a minimal prominence ($p_{\min} = 0.1$). The prominence of a peak measures how much a peak is emerging clearly locally in the signal. It is defined as the vertical distance between the peak and the altitude of the largest region it dominates. These values were found to yield best peak interpretations over the whole set of TFs. We used the function `scipy.signal.find_peaks` of the `scipy` library.

Positive cell clusters (Step 5): For each TF, the average number “ p ” of positive cells was computed in each Lin A/15 iMN observed Cluster. The procedure varied according to whether only one peak was detected or more than one (*i.e.* 2 in our data).

Case of a single detected peak (*e.g.* Jim): The altitude of the peak at which the signal width below the peak is exactly “ p ”. The cluster of positive cells was assumed to correspond to all the cells expressing the TF.

Case of two detected peaks (*e.g.* oli).

The sequence was split into the regions defined by each peak. Then the average number of positive cells “ p_1 ” and “ p_2 ” are computed for each of the two regions. Then the method proceeds within each region and its average number of positive cells as in the case of a single detected peak. This determines both the estimated length and the position of the two positive cell clusters.

The method leaves some uncertainty as to whether a cell located at the boundary of the cluster coverage (Step 6) should or not be considered as positive. If we consider that a cell at integer position x extends from $x-0.5$ to $x+0.5$, we can define a coverage index at the border (number from 0 to 1), revealing how much the positive cell cluster falls into the region around the cell (at -0.5 to $+0.5$).

For example, the length of the Jim positive cell cluster is 8.2 and its position is [14.8–23.1], which makes the two cells, cell 15 (14.8 belongs to [15–0.5, 15 + 0.5]) and cell 23 (23.1 belongs to [23–0.5, 23 + 0.5]), situated at the boundary uncertain of Jim expression. The coverage index is thus calculated for both cells, 0.7 (*i.e.*: 15.5–14.8) for cell 15 and 0.6 (*i.e.*: 23.1–22.5) for cell 23 (Figure 2). Since the average number of cells expressing Jim is 8.3, either cell, other than both, could be considered as positive and the method cannot distinguish between them. The coverage index at the border is indicated for cell cluster when inferior to 1.

Test of the PCCD method by co-staining

The cell cluster detection method predicts the combinations of TFs expressed in each immature MN. To validate the positive-cell cluster detection method and to determine its accuracy, we tested its predictions by performing co-stainings. Among 256 possible co-stainings, we chose $N = 12$ co-staining combinations, serving as a proof-of-concept. We chose those combinations to test two parameters of the positive-cell cluster detection method: the accuracy of the position of the positive-cell cluster and the accuracy of the number of cells per cluster when 2 cell clusters were detected (length of the positive cell cluster).

The accuracy of the position of the positive cell cluster:

The number of cells expressing a given TF (length of the positive-cell cluster) is not a prediction of the model when only one cluster is detected because this parameter is based on real data: average number of positive cells expressing a given TF from all our experiments. However, we tested the accuracy of the position on the x' axis of the positive-cell cluster by performing co-staining between TFs that have partially overlapping cluster coverage.

Kr and Zfh2 co-staining

Prediction of the PCCD: The model predicts 3 to 5 cells expressing both TFs with a higher probability of only 3 cells because there is a higher chance for cell #5 rather than cell #1 to express Kr (coverage index at cell #5 for Kr is 0.9 and 0.4 at cell #1) and low chance for cell #5 to express Zfh2 (coverage index at cell #5 for Zfh2 is 0.3). Result of the co-staining: Number of cells expressing Kr and Zfh2 = 3. We concluded, as predicted by the model, that cell #5 expresses Kr whereas cell #1 did not, and cell #5 is Zfh2 negative.

Lov and Zfh2 co-staining

Prediction of the PCCD: The model predicts 1 to 3 cells expressing both TFs with a higher probability of 2 cells because there is higher chance for cell #3 rather than cell #7 to express Lov (coverage index at cell #3 for Lov is 0.6 and 0.4 at cell #7) and low chance for cell #5 to express Zfh2 (coverage index at cell #5 for Zfh2 is 0.3). Result of the co-staining: Number of cells expressing Lov and Zfh2 = 2. Lov antibody seems to be sensitive to fixation conditions and we found one more cell expressing low level of Lov after optimizing the fixation conditions (Figure S2). Consequently, we corrected the length of the positive cell cluster of Lov from 4 to 5 and included both cell #3 and cell #7. We included cell #3 as the cell expressing low level of Lov because the cell expressing a low level of Lov is Zfh2+.

Chinmo and Jim co-staining

Prediction of the PCCD: The model predicts to have 3 to 5 cells expressing both TFs. Result of the co-staining: Number of cells expressing Chinmo and Jim = 4. Here, we have two possibilities: cell #15 is Jim+ and cell #19 is Chinmo- or cell #15 is Jim- and cell #19

is Chinmo+. In the PCCD method the length of the positive cell cluster of Chinmo is 18.5. After including the Chinmo + cells from co-staining experiments the average number of cell expressing Chinmo is closer to 19. This variation between samples is due to the weak expression of Chinmo in one Jim + cell localized ventrally, which is sometimes not detected (Figure S2). We thus concluded that cell #23 expresses Jim while cell #15 does not.

Conclusion: the combinatorial expression of TFs predicted by the method seems to be accurate since the co-staining validated the predictions.

The number of cells per cluster when 2 cell clusters are detected (length of positive cell cluster) and accuracy of the position of the positive cell cluster.

We tested the length of the positive dorsal cluster (left cluster) when two clusters were detected, by performing co-staining between TFs that were predicted to be completely overlapping in the dorsal cluster and not the ventral one. We then tested the accuracy of the position of the positive cell cluster as described in the previous paragraph. We tested the length, as well as the position, of cell clusters expressing RunxA, Zfh1, Oli and Nvy.

RunxA and chinmo co-staining (testing the length of the dorsal RunxA + cluster)

Prediction of the PCCD: The model predicts a length of the dorsal RunxA + cluster = 5.1 and a number of cells expressing RunxA and Chinmo = 5. Result of the co-staining: Number of cells expressing RunxA and Chinmo = 5. We concluded that the number of cells expressing RunxA in the dorsal is cluster is correct.

RunxA and jim co-staining (testing the position of the dorsal RunxA + cluster)

Prediction of the PCCD: The model predict 0 to 1 cell expressing both. Result of the co-staining: Number of cells expressing RunxA and Jim = 0. Because we demonstrated in the previous paragraph that cell #15 is Jim-, we could not conclude if the cell #10 or the cell #15 is RunxA+.

Zfh1 and chinmo co-staining (testing the length of the dorsal Zfh1+ cluster)

Prediction of the PCCD: The model predicts a length of the dorsal Zfh1+ cluster = 10.8 and a number of cells expressing Zfh1 and Chinmo = 10 or 11. Result of the co-staining: Number of cells expressing Zfh1 and Chinmo = 12. Based on these results, we made a correction of the length of the dorsal Zfh1+ cluster from 10.8 to 12.

Zfh1 and Zfh2 co-staining (testing the position of the dorsal Zfh1+ cluster)

Prediction of the PCCD: The model predicted 2 to 4 cells expressing both TFs. Result of the co-staining: Number of cells expressing Zfh1 and Zfh2 = 2. We concluded that cell #2 does not express Zfh1 and cell #5 does not express Zfh2.

Zfh1 and Kr co-staining (testing the position of the dorsal Zfh1+ cluster)

Prediction of the PCCD: The model predicts 2 to 4 cells expressing both TFs. Result of the co-staining: Number of cells expressing Zfh1 and Kr = 3. We had concluded (from Kr and Zfh2 co-staining) that cell #5 is Kr+, confirming that cell #2 does not express Zfh1.

Based on these three co-stainings including Zfh1, we concluded that cell #13 expresses Zfh1 while cell #2 does not. Moreover, we made a correction by adding cell #14 into the Zfh1+ cluster to respect a length of the Zfh1+ cluster = 12.

Oli and Zfh2 co-staining (testing the length of the dorsal Oli + cluster)

Prediction of the PCCD: The model predicts a length of the dorsal Oli + cluster = 2.8 and a number of cells expressing Oli and Zfh2 = 2 or 3. Result of the co-staining: Number of cells expressing Oli and Zfh2 = 2. Based on these results we made a correction of the length of the of Oli + cell cluster for the first Oli cluster. The length of the Oli + cell cluster = 2 instead of 2.8.

Oli and Kr co-staining (testing the position of the dorsal Oli + cluster)

Prediction of the PCCD: The model predicts to have 1 to 3 cells expressing both. Result of the co-staining: Number of cells expressing Oli and Kr = 1. We concluded that cell #1 expresses Oli whereas cell #3 does not.

Nvy and Chinmo (testing the length of the dorsal Nvy + cluster)

Prediction of the PCCD: The model predicts a length of the dorsal Nvy + cluster = 3.6 and a number of cells expressing Nvy and Chinmo = 3 or 4. Result of the co-staining: Number of cells expressing Nvy and Chinmo = 4. Notably, we notice that the dorsal Nvy + cluster express higher level of nvy compare to the ventral cluster.

Nvy and Jim (testing the position of the dorsal Nvy + cluster)

Prediction of the PCCD: The model predicts 0 to 2 cells expressing both TFs. Result of the co-staining: Number of cells expressing Nvy and Jim = 2. However, these two cells express a very low level of Nvy and are located ventrally in the 14 samples analyzed. We concluded that cell #12 instead of #16 is Nvy+. See below for comments on the ventral clusters and why the PCCD method did not predict that 2 cells of the ventral Nvy + cluster express Jim.

Conclusion: The length of the cluster coverage when two clusters are detected, is accurate. No corrections or sometimes corrections of one cell to cluster length were made.

Note for the ventral clusters: The PCCP method probably underestimated the number of cells that should be included on the left region of clusters located near the NB. Indeed, the frequency of TF expression in a cell close to the NB was low, not because of the variation in the cell positioning between samples, but due to the fact that the cell may not have been born in some samples. This would artifactually reduce the frequency of TF expression at positions close to the NB. This bias could be overcome in a future version of the PCCD method. However, the Nvy and Jim co-staining revealed that the errors were small. Finally, all ventral clusters had a gradient expression from high (ventral) to low (dorsal). Consequently, the boundary of the left region of these clusters was not sharp due to weak TF expression that was sometimes difficult to detect.

Lin A/15 MARCM clones vs Lin A/15 memory system

The one-spot MARCM technique makes it possible to visualize one of the daughter cells derived from a common progenitor (Lee and Luo, 1999). Consequently, the generation of an NB MARCM Lin A/15 clone at the larval stage, when the NB is quiescent, makes it possible to visualize the first MN born or the next 28 MNs, but not all together. However, the Lin A/15 memory system (Awasaki et al., 2014; Lacin and Truman, 2016) allows the visualization of all 29 MNs.

Link between birth order and muscle targets: Corrections of (Baek and Mann, 2009)

A previous study revealed a link between the Lin An MN birth order and the muscles they target (Baek and Mann, 2009). In our study (Figure 1), we made two corrections by adding two MNs (Lin A Tr1 and B1), not described in (Baek and Mann, 2009). The relative birth orders of the 28 Lin A/15 MNs have been characterized by inducing GMCs MARCM clones at different time points during larval stages. The generation of GMC MARCM clones has allowed the determination of the relative birth order of 27 MNs out of the 28 MNs. In our study, when we generated an NB MARCM clone to label the 28 Lin A/15 MNs, we always marked an MN targeting the trochanter segment, an MN which was not considered to be part of Lin A/15 (Baek and Mann, 2009). We named this MN, Lin A/15 Tr1. Based on the shape of the axonal terminal branches, we propose that this MN has been misidentified (Baek and Mann, 2009) as Lin G, a lineage supposedly producing a single MN. Here, we propose that Lin G is not a lineage by itself (discovered by generating an NB MARCM clone) but a GMC MARCM clone. Moreover, we conclude that Lin A/15 Tr1 MN is the first born MN of the 28 MNs by comparing in the Baek and Mann article (2009), the last time point where the Tr1 GMC MARCM clone can be induced with the other GMC MARCM clones. Finally, the NB one-spot MARCM technique, cannot label the first Lin A/15 MN. The twin spot QMARCM/MARCM has revealed that the first-born MN from Lin A/15 targets a body wall muscle (Enriquez et al., 2018). Here, we name this MN: B1.

QUANTIFICATION AND STATISTICAL ANALYSIS

Graphs of the relative position of each LinA/15 cell were generated with Microsoft Excel. The spatial coordinates were assigned to each cell using the cell counter plug-in of NIH ImageJ software. The coordinates of each cell were normalized with Microsoft Excel in order to have the position of the Lin A/15 NB at the origin of the plot graph. For samples where the NB was not labeled, the coordinates of each cell were then normalized to a cell located most anteriorly.

The plots of the number of TF-expressing cells (TFs are as indicated in each graph) were generated with Prism (GraphPad Software). All error bar represents standard deviation of a minimum of 7 Lin A/15 samples, each dot represents a single Lin A/15 sample analyzed. Student's t test was performed to compare the difference in between indicated groups. Differences of $p < 0.05$ were considered significant. * $0.01 < p < 0.05$; ** $0.001 < p < 0.01$; *** $0.0001 < p < 0.001$, **** $p < 0.0001$.